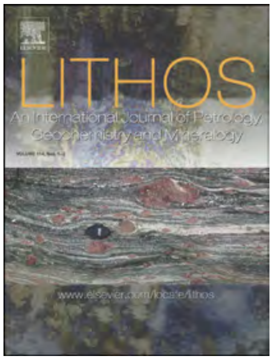

Olivine compositional changes in primitive magmatic skarn environments: A reassessment of divalent cation partitioning models to quantify the effect of carbonate assimilation

Flavio Di Stefano, Silvio Mollo, Piergiorgio Scarlato, Manuela Nazzari, Olivier Bachmann, Marco Caruso

PII:	S0024-4937(18)30240-8
DOI:	doi:10.1016/j.lithos.2018.07.008
Reference:	LITHOS 4714
To appear in:	*LITHOS*
Received date:	8 February 2018
Accepted date:	5 July 2018

Please cite this article as: Flavio Di Stefano, Silvio Mollo, Piergiorgio Scarlato, Manuela Nazzari, Olivier Bachmann, Marco Caruso , Olivine compositional changes in primitive magmatic skarn environments: A reassessment of divalent cation partitioning models to quantify the effect of carbonate assimilation. Lithos (2018), doi:10.1016/j.lithos.2018.07.008

Olivine compositional changes in primitive magmatic skarn environments: A reassessment of divalent cation partitioning models to quantify the effect of carbonate assimilation

Flavio Di Stefano[1,*], Silvio Mollo[1,2], Piergiorgio Scarlato[2], Manuela Nazzari[1,2], Olivier Bachmann[3], Marco Caruso[1]

[1]Dipartimento di Scienze della Terra, Sapienza-Università di Roma, P.le Aldo Moro 5, 00185 Roma, Italy

[2]Istituto Nazionale di Geofisica e Vulcanologia, Via di Vigna Murata 605, 00143 Rome, Italy

[3]Department of Earth Sciences, Institute of Geochemistry and Petrology, ETHZ, Clausiusstrasse 25, 8092 Zurich, Switzerland

***Corresponding author:**
Dr. Flavio Di Stefano
Dipartimento di Scienze della Terra,
Sapienza-Università di Roma,
P.le Aldo Moro 5,
00185 Roma, Italy
Email: flavio.distefano@uniroma1.it

Abstract

The geochemical evolution of olivine from primitive magmatic skarn environments has been studied by atmospheric pressure experiments carried out at 1,250, 1,200, and 1,150 °C under QFM oxygen buffering conditions. The starting materials were three synthetic basalts (i.e., $^{melt}Mg\#_{78}$, $^{melt}Mg\#_{75}$, and $^{melt}Mg\#_{72}$) doped with variable amounts of $CaCO_3$, in order to reproduce the natural concentration levels of CaO-rich magmas interacting with the skarn rock shells. Results from decarbonation experiments evidence that the crystallization of Fo-CaO-rich, NiO-poor olivines is more favored at higher temperatures when primitive basaltic magmas assimilate increasing amounts of carbonate materials. The number of large size Ca cations entering olivine crystal lattice is proportional to the amount of Ca-O-Si bonds available in the melt. Due to differences between Fe^{2+} and Mg cation radii, the Ca-Fe^{2+} substitutions into M2 crystallographic site are more facilitated than Ca-Mg ones, thus enhancing the forsterite component in olivine. The partitioning behavior of Ni, Mg, Fe^{2+}, Mn, and Ca between olivine and melt has been also investigated to better understand cation redistribution mechanisms at the magma-carbonate reaction zone. In this context, some partitioning models from the literature have been refined to more accurately quantify the geochemical evolution of primitive skarn systems. Under the effect of $CaCO_3$ assimilation, the partitioning of divalent cations, can be parameterized as a function of temperature, bulk composition (mostly, CaO and MgO contents in both olivine and melt) and melt structure (expressed as the number of non-bridging oxygens per tetrahedrally coordinated cations). Conversely, the exchange partition coefficients between Fe^{2+}/Ca/Mn/Ni and Mg do not vary significantly as a function of temperature and $^{melt}Mg\#$, due to the limited influence of these parameters on the melt structure. In turn, cation exchange reactions are primarily controlled by the strong depolymerizing effect of $CaCO_3$ assimilation that increases the number of structural sites critically important to accommodating network-modifying cations in the melt phase. The comparison between cumulates and magmatic skarns from the Colli Albani Volcanic District (Italy) and experiments from this study provides quantitative constraints on the geochemical evolution of olivine phenocrysts and their melt inclusions as a function of carbonate assimilation.

Keywords: olivine; partition coefficients; carbonate assimilation; primitive magmatic skarn environment

1. Introduction

Crustal contamination may significantly contribute to the differentiation path of magma (DePaolo, 1981; Foland et al., 1993; Patiño Douce, 1999; Spera and Bohrson, 2001, 2004; Barnes et al., 2005; Mollo et al., 2011; Del Bello et al., 2014). This is particularly true during magma-carbonate interaction which is characterized as a multi-stage reaction zone advancing from the carbonate wall-rock towards the innermost part of the magma chamber (Wenzel et al., 2002; Gaeta et al., 2009; Mollo et al., 2010; Di Rocco et al., 2012; Mollo and Vona, 2014). The interaction mechanism is generally associated with the formation of three distinct skarn domains (Di Rocco et al., 2012): (1) exoskarns i.e., thermometamorphic rocks derived by decarbonation of the protolith, (2) endoskarns i.e., magmatic rocks derived by crystallization and desilication phenomena at the exoskarn-magma interface, and (3) cumulates i.e., highly crystalline rocks derived by magma contamination and crystal accumulation at the endoskarn-magma interface. The principal products of carbonate thermal decomposition are the formation of CaO-rich melts and the release of CO_2 (Deegan et al., 2010; Mollo et al., 2010, 2011, 2013a; Freda et al., 2011). This latter has important implications for anomalously high CO_2 degassing rates currently estimated at several continental arc volcanoes. Indeed, in mature continental arcs reworking of crustal limestone by hot mafic magmas may be an important source of CO_2 flux (Mason et al., 2017). For example, Carter and Dasgupta (2015) have shown that magma-induced upper plate decarbonation alone may potentially contribute to the excess of CO_2 released into the atmosphere (i.e., up to ~3% of the current global arc CO_2 flux may be crustally derived). Further experimental data have also illustrated that melt composition and melt fraction are effective controlling factors in the transition from assimilation to skarnification, and that both heat and aqueous fluids released from an intruding magma may enhance significantly CO_2 degassing (Carter and Dasgupta, 2016).

During magma-carbonate interaction, the exoskarn domain is characterized by low temperature, metamorphic/metasomatic reactions where the oxidative capacity of CO_2-rich fluids

(X_{CO2}>0.99) leads to high oxidation conditions (≥MH buffer; Di Rocco et al., 2012). The endoskarn domain is governed by significant magma cooling and differentiation under moderate-to-high oxidation conditions (≥NNO buffer; Wenzel et al., 2002). The abundant crystallization of CaTs-rich clinopyroxene phenocrysts (Mollo et al., 2010; Carter and Dasgupta, 2015) produces silica-poor, alkali-rich magmas typical of ultrapotassic volcanism (Gaeta et al., 2009). The cumulate domain represents the primitive skarn environment where high temperature, less oxidized (~QFM buffer), primitive magmas fractionate Fo-rich olivine phenocrysts accumulating at the base and periphery of the magma chamber (Di Rocco et al., 2012). Considering the temporal and spatial relationships between exoskarns, endoskarns, and cumulates, the occurrence of olivine as liquidus phase and its compositional evolution are strictly dependent on the progressive advancement of the magma-skarn interface, the thermal (differentiation) path of the system, and the degree of CaO contamination (Wenzel et al., 2002; Barnes et al. 2005; Chadwick et al., 2007; Coulson et al., 2007; Freda et al., 2008; Iacono Marziano et al., 2008; Gaeta et al., 2009; Di Rocco et al., 2012; Jolis et al., 2015). In this scenario, the overall skarn environment acts as a continuous source of CO_2 gas phase and CaO-rich melts that variably interact with primitive basaltic magmas, thus controlling their geochemical evolution under olivine-saturated to olivine+clinopyroxene-cosaturated to clinopyroxene-saturated conditions (cf. Gaeta et al., 2009).

The purpose of this study is to experimentally investigate the early stage of carbonate assimilation when high temperature, primitive basaltic magmas assimilate variable amounts of carbonate material and then equilibrate with olivine phenocrysts. These experimental data allow to better constrain the effect of CaO contamination on the evolutionary behavior of the primitive magmatic skarn environment that is represented by the endoskarn domain. The partitioning of divalent cations (i.e., Ni, Mg, Fe, Mn, and Ca) between olivine and melt has been also investigated due to its importance in estimating the solidification temperature of rocks (e.g., Hart and Davis, 1978; Ford et al., 1983; Beattie, 1993; Putirka 2005, 2008; Putirka et al., 2007, 2011; Wang and Gaetani, 2008; Li and Ripley, 2010; Matzen et al., 2013; Pu et al., 2017), in ascertaining the equilibrium condition of minerals (e.g., Roeder and Emslie, 1970; Leeman and Scheidegger, 1977; Snyder and Carmichael, 1992; Putirka 2005, 2016; Toplis, 2005; Filiberto and Dasgupta, 2011), and in understanding magmatic processes (e.g., Danyushevsky and Plechov, 2011; Mollo et al., 2015). In this context, several olivine-melt partitioning equations published over the last decades have been collected and integrated all together into an Excel spreadsheet submitted online as supplementary material (Hart and Davis, 1978; Beattie et al., 1991; Snyder and Carmichael, 1992; Beattie, 1993; Jones, 1995, 2016; Libourel, 1999; Putirka, 2005, 2016; Toplis, 2005; Putirka et al., 2007, 2011; Wang and Gaetani, 2008; Pu et al., 2017). The equations more suitable for modeling decarbonation data from this study have been selected, discussed and reappraised in terms of temperature and compositional variations during magma-carbonate interaction. More specifically, the predictive ability of these equations has been improved by including compositional parameters that more accurately describe the variance of the data obtained from decarbonation experiments.

2. Starting materials, experimental conditions and analytical methods

Three different basaltic starting materials were synthesized in batches of ~2 g from pure oxides and carbonates mixed by grinding under ethanol in an agate mortar for ~1 h. These mixtures were chosen in order to obtain three basalts with different primitive characters of $^{melt}Mg\#_{72}$, $^{melt}Mg\#_{75}$, and $^{melt}Mg\#_{78}$ [$^{melt}Mg\# = X_{MgO} / (X_{MgO} + X_{FeO}) \times 100$, where X_{FeO} refers to FeO recalculated at the QFM buffer, according to the formula of Kress and Carmichael (1991)] (Table 1S). Ni was added to the powdered mixture as solution with nominal concentration of 1,000 ppm. To guarantee obeyance of Henry's Law (Mysen 2006), the Ni concentration is similar to that observed in natural basaltic rocks (cf. Mollo et al., 2013b). A Fe pre-saturated Pt-crucible containing the synthetic powder was loaded in a 1 atm vertical tube CO–CO_2 gas-mixing furnace at the quartz-fayalite-magnetite (QFM) buffer. Melting experiments were conducted at the HP-HT Laboratory of Experimental Volcanology and Geophysics of the Istituto Nazionale di Geofisica e Vulcanologia (INGV) in Rome, Italy. The temperature was kept at 900 °C for 1 h to ensure decarbonation and, then, was raised up to 1,600 °C and kept for 1 h to ensure melting and to obtain glass starting material. The resulting glass was removed from the Pt-crucible and, then, powdered. Backscattered images and microprobe analyses performed on chips extracted from top, middle, and bottom of the Pt-crucible, demonstrated homogeneity and the absence of crystalline phases. In order to minimize loss of transition metals, some aliquots of the powder were previously loaded into the Pt-crucible and run for 3 h at 1,600 °C to saturate the crucible (cf. Conte et al., 2006). The sample holder was then quenched and cleaned in a hot HF solution. The same approach was adopted to saturate the Pt-wire (0.1 mm in diameter) used for the equilibrium experiments conducted at 1 atm and the QFM buffer. Through this strategy, the Fe loss from the samples was kept to <5% of the initial amount. Notably, all the experiments were carried out at 1 atm on the basis of the following considerations: i) our magma-carbonate interaction experiments can be more properly compared with previous studies investigating and modeling the partitioning of divalent cations between olivine and melt at ambient pressure (e.g., Roeder and Emslie, 1970; Leeman and Scheidegger, 1977; Hart and Davis, 1978; Snyder and Carmichael, 1992; Kohn and Schofield, 1994; Jones, 1995, 2016; Beattie, 1993; Libourel, 1999; Wang and Gaetani, 2008), ii) olivine is always the liquidus phase and its stability field increases at the expense of clinopyroxene (Snyder and Carmichael, 1992; Mollo et al., 2015), iii) cation exchange reactions in olivine do not substantially change from low to moderate crustal depths (e.g., Roeder and Emslie, 1970; Takahashi, 1978; Sack et al., 1987; Gee and Sack, 1988; Kushiro and Mysen, 2002; Toplis, 2005; Matzen et al., 2011), and iv) the effect of H_2O and P_{H2O} on olivine stability is practically negligible in primitive magmatic skarn environments due to the strong amount (~45 wt.%) of CO_2 released during calcite thermal decomposition (Wenzel et al., 2002; Di Rocco et al., 2012). The equilibrium temperature was measured by a Pt–$Pt_{90}Rh_{10}$ thermocouple located within 1 cm of the sample chandelier holding the experimental Pt-loops (about 1.5 mm in diameter) charged with about 45 µg of powdered starting material (cf. Mollo and Vona, 2014). The oxygen fugacity was monitored and maintained constant over the experimental temperatures of 1,150, 1,200 and 1,250 °C by means of an yttria-dopedzirconia solid electrolyte oxygen sensor ($SIRO_2$, Ceramic Oxide Fabricators, Ltd., Australia) and two digital thermal mass flow meters (for CO and CO_2) controlled via software. The $^{melt}Mg\#_{72}$, $^{melt}Mg\#_{75}$, and $^{melt}Mg\#_{78}$ basaltic powders were also doped with 0, 10, and 20 wt.% of $CaCO_3$ in order to obtain total CaO contents of ~11, ~16, and ~22 wt.%, respectively. At a given experimental temperature, three Pt-loops containing basalts with the same $^{melt}Mg\#$ but different CaO contents were simultaneously suspended within the furnace. The superliquidus temperature of 1,300 °C was reached in 1 h starting from room temperature and it was maintained for 0.5 h before beginning cooling. It was experimentally verified that no crystalline phases formed during thermal pre-treatment at 1,300 °C. The samples were cooled at a rate of 30 °C/h from 1,300 °C down to the final target temperature that was kept constant for 72 h. Each experiment was fast-quenched by dropping the charge into a water bath. The run product was mounted in epoxy, and a polished thin section was produced from the epoxy block. According to previous reversal and cooling rate experiments conducted by Mollo et al. (2013b, 2013c) on similar basalts, the experimental duration of 72 h is sufficient to ensure the achievement of mineral-melt chemical equilibrium and ferric–ferrous equilibration in the melt at atmospheric pressure. Vetere et al. (2013) have also demonstrated that the relaxation kinetics of basaltic melts are extremely rapid in time (i.e., from milli- to micro-seconds) and independent of the superheating paths used in laboratory.

Major oxide analyses of experimental products were performed with a Jeol-JXA8200 EDS-WDS combined electron microprobe equipped with five wavelength-dispersive spectrometers and installed at the HP-HT Lab of INGV. The analytical conditions were 15 kV accelerating voltage and 10 nA beam current, 5 µm beam diameter, and 20 s counting time. The following standards were adopted for the various chemical elements: jadeite (Si and Na), corundum (Al), forsterite (Mg), andradite (Fe), rutile (Ti), orthoclase (K), barite (Ba), apatite (P), spessartine (Mn) and metallic nickel (Ni). Sodium and potassium have been analyzed first to reduce possible volatilization effects. The precision of the microprobe was measured through the analysis of well-characterized synthetic oxides and minerals. Data quality was ensured by analyzing standard materials as unknowns based on counting statistics, analytical precision and accuracy were better than 5% for all cations (Tables 2S and 3S).

The Ni concentration (at ppm levels) in the residual glass was too low to be accurately measured via microprobe. Thus, further analyses were performed at the Institute of Geochemistry and Petrology of the ETH Zürich, Switzerland. Data were collected through a 193 nm excimer laser coupled with a second generation two-volume constant geometry ablation cell (Resonetics:S-155LR) and a high-sensitivity, sector-field inductively-coupled plasma mass spectrometer (ICP-MS; Thermo:Element XR). Points with a spot size of 13 μm were set on chemically homogeneous portions of the material previously analyzed by electron microprobe, and ablated with a pulse rate of 10 Hz and an energy density of 3.5 J/cm^3 for 40 sec. The isotope was analyzed relative to an internal standard of known composition (i.e., NIST612). A second standard (i.e., GSD-1G) was used as an unknown to check the quality of data during each analytical run. ^{29}Si was used as internal standard. The analytical precision corresponds to the 1 sigma errors calculated from variations in replicate analyses that resulted invariably greater than the fully integrated 1 sigma errors determined from counting statistics alone.

3. Results

3.1. Phase relations and abundances

Olivine, clinopyroxene, titanomagnetite, and glass occur in the experimental charges, showing variable proportions as a function of temperature, starting melt composition (i.e., ^{melt}Mg#), and degree of $CaCO_3$ assimilation (Table 1). Modal phase abundances have been derived by mass balance calculations (Table 1), yielding relative low residual sum of squares ($\Sigma r^2 < 0.75$). This points to a fairly good conservation of mass relative to the chemical analyses of crystals and glasses, suggesting (near-)equilibrium crystallization conditions (Stormer and Nicholls, 1978). The most important features of the experimental charges can be schematized as follows (Table 1): i) olivine saturates the basaltic melt in all the experimental charges, ii) the amount of olivine is maximum (12%) in the most primitive $^{melt}Mg\#_{78}$ experimental charge and decreases with increasing $CaCO_3$ assimilation, iii) at 1,250 °C, clinopyroxene is always absent, irrespective of the starting melt composition (i.e., $^{melt}Mg\#$) and the amount of $CaCO_3$ assimilated, iv) at 1,200 °C, clinopyroxene does not crystallize from the undoped experimental charges ($^{melt}Mg\#_{78}$, $^{melt}Mg\#_{75}$, and $^{melt}Mg\#_{72}$) but occurs in the most differentiated $^{melt}Mg\#_{72}$ basalt doped with 10 and 20 wt.% $CaCO_3$, v) at 1,150 °C, clinopyroxene is ubiquitous in basalts assimilating 20 wt.% $CaCO_3$ and its modal content increases from ~9% to ~20%, as the melt composition shifts from $^{melt}Mg\#_{78}$ to $^{melt}Mg\#_{72}$, vi) titanomagnetite is extremely rare (~1%), appearing only at 1,150 °C in the most differentiated $^{melt}Mg\#_{72}$ basalt, vii) at 1,250 °C, olivine nucleates and grow as large, euhedral, and isolated crystals showing regular planar faces and lengths up to ~3 mm, and viii) at 1,150 °C, an intricate network of elongated crystals occurs, due to the enlargement of the stability field of clinopyroxene at the expense of olivine (see mineral proportions in Table 1).

3.2. Glass chemistry

The glass analyzed around olivine and clinopyroxene is chemically homogeneous (Table 2S), attesting that chemical nutrients were supplied to the growing crystals at equilibrium proportions (note that equilibrium values have been derived for the Fe^{2+}-Mg exchange reaction between olivine and melt; see discussion below). As the temperature decreases, the glass composition remains almost constant in terms of SiO_2, whereas Na_2O+K_2O increase with olivine and clinopyroxene crystallization (Table 2S). The most important chemical variations occur as a function of $CaCO_3$ assimilation, causing melt desilication (i.e., SiO_2 decreases from ~52 to ~43 wt.%) and decarbonation (i.e., CaO increases from ~11 to ~22 wt.%), in agreement with what observed in previous studies (Fulignati et al., 2000; Gaeta et al., 2009; Mollo et al., 2010; Di Rocco et al., 2012; Gozzi et al., 2014; Mollo and Vona, 2014; Ammannati et al., 2016). Residual glasses from the most primitive $^{melt}Mg\#_{78}$ basalt are characterized by the highest contents of CaO, TiO_2, Al_2O_3, and MnO (Table 2S), corresponding to the lowest degree of clinopyroxene crystallization

(Table 1). In contrast, the concentrations of FeO, Na_2O, and K_2O are maximum in the residual glasses formed from the most evolved clinopyroxene-saturated $^{melt}Mg\#_{72}$ starting composition (Table 2S). The TAS (total alkali vs. silica; Le Bas et al., 1986) diagram classifies the residual glasses as basalt-basaltic andesite (from 0 to 10 wt.% $CaCO_3$ assimilation) and basanite-tephrite (20 wt.% $CaCO_3$ assimilation).

3.3. Mineral chemistry

Olivine is the liquidus phase in all the experimental charges and its chemistry varies considerably as a function of the experimental conditions (Table 3S). As the temperature decreases, MgO is less favorably incorporated into olivine crystal lattice, whereas the opposite occurs for FeO, MnO, NiO, and CaO (Fig. 1). The most primitive $^{melt}Mg\#_{78}$ basalt forms olivines with the highest MnO, MgO, and CaO concentrations and the lowest FeO and NiO contents (Fig. 1). With increasing $CaCO_3$ assimilation, olivine shows MgO and CaO enrichments, counterbalanced by FeO, MnO, and NiO depletions. Olivines with CaO contents up to 2.33 wt.% are consistent with those (1.31–2.36 wt.% CaO) equilibrated by previous magma–carbonate interaction experiments conducted on basaltic to shoshonitic compositions doped with $CaCO_3$ amounts variable from 5 to 20 wt.% (cf. Conte et al., 2009; Mollo et al., 2010; Jolis et al., 2013). In order to compare olivine components from this study with those reported in literature (e.g., Wenzel et al., 2001, 2002; Gaeta et al., 2009; Iacono Marziano et al., 2009; Dallai et al., 2011; Di Rocco et al., 2012; Gozzi et al., 2014; Hayes et al., 2015; Redi et al., 2017), the mineral stoichiometry has been calculated in Table 3S as a simple solid solution of forsterite (Fo; Mg_2SiO_4) and fayalite (Fa; Fe_2SiO_4), following the same method adopted by previous authors. The maximum Fo_{93} content is measured for crystals from the primitive $^{melt}Mg\#_{78}$ basalt assimilating 20 wt.% of $CaCO_3$ at 1,250 °C (Table 3S). The Fo content decreases from 93 to 87 with decreasing $^{melt}Mg\#$, temperature, and $CaCO_3$ (Table 3S). For the sake of completeness, a more comprehensive solution model for olivine components has been also used in this study, by considering forsterite, fayalite, larnite or calcio-olivine (Ca-ol; Ca_2SiO_4), and tephroite (Teph; Mn_2SiO_4) as end-members (see Table 3S). This strategy allows to better evidence that, with increasing $CaCO_3$ assimilation, Fo and Ca-ol remarkably increase at the expense of Fa and Teph (Fig. 2).

The clinopyroxene chemistry closely resembles that already discussed in previous experimental works (Mollo et al., 2010; Mollo and Vona, 2014), showing preferential enrichments in TiO_2, Al_2O_3, FeO, and CaO during $CaCO_3$ assimilation, in concert with a remarkable depletion in MgO (Table 4S). The molecular proportions of Ca-Tschermak (CaTs, $CaAl_2SiO_6$), CaFe-Tschermak (CaFeTs; $CaFeSiAlO_6$), and CaTi-Tschermak (CaTiTs, $CaTiAl_2O_6$) are observed to increase from 0.08 to 0.11, from 0.01 to 0.03, and from 0.05 to 0.07, respectively. In contrast, diopside (Di, $CaMgSi_2O_6$) and enstatite (En, $Mg_2Si_2O_6$) decrease from 0.51 to 0.45 and from 0.07 to 0.02, respectively (Table 4S).

Magnetite, which appears only in the most evolved ${}^{melt}Mg\#_{72}$ basalt equilibrated at 1,150 °C, shows an increase of Al_2O_3, FeO_{tot}, MnO, and MgO with increasing $CaCO_3$, as well as a likewise decrease of TiO_2 (Table 5S). Consequently, the ulvospinel (Usp, $TiFe_2O_4$) component is observed to decrease from 0.36 to 0.14 (Table 5S).

4. Discussion

4.1. Geochemical evolution of olivine in primitive magmatic skarn environments

Relative to the formation of natural magmatic skarn environments (Dunworth and Wilson, 1998; Battistini et al., 2001; Wenzel et al., 2001, 2002; Gaeta et al., 2009; Dallai et al., 2011; Di Rocco et al., 2012; Del Bello et al., 2014; Gozzi et al., 2014; Redi et al., 2017), data from this study allow to better understand the geochemical evolution of olivine (Figs. 1 and 2) from the interior of the magma chamber (i.e., uncontaminated basalt) towards the carbonate wall-rock (i.e., contaminated basalt). This makes also possible to quantify the complex interplay between temperature and bulk compositional changes during magma cooling, crystallization, and carbonate assimilation. For example, at the highest temperature of 1,250 °C, clinopyroxene does not crystallize from $^{melt}Mg\#_{78}$ and $^{melt}Mg\#_{72}$ basalts, even if the degree of assimilation increases by up to 20 wt.% $CaCO_3$. Therefore, at high temperature, olivine is energetically more favored than clinopyroxene (Table 1). The composition of olivine shifts from Fo_{87} to Fo_{93} when the melt desilication proceeds from 50 to 42 wt.% SiO_2 with increasing $CaCO_3$. This is consistent with the chemistry (Fo_{88-91}) of natural olivine phenocrysts from cumulate and endoskarn rocks formed at the early stage of carbonate assimilation by basaltic magmas (Dunworth and Wilson, 1998; Wenzel et al., 2001, 2002; Gaeta et al., 2009; Dallai et al., 2011; Di Rocco et al., 2012; Gozzi et al., 2014; Redi et al., 2017). Natural products are generally characterized by orthocumulate to mesocumulate to adcumulate textures (Irvine, 1982), resulting from the aggregation of mafic crystals in a reaction-cumulate zone at the periphery of the magma chamber, where CaO-rich melts are persistently extracted from the skarn rock shells (Wenzel et al., 2002). More specifically, primitive skarn-bearing dunite cumulates result from high temperature reactions commencing at 1,200-1,260 °C and oxygen fugacity close to QFM buffer (Wenzel et al., 2002). Under such circumstances, the activity of CaO and the Fe speciation in the pristine melt facilitate the incorporation of Ca cations into the more stable (i.e., Fe^{2+}-bearing) olivine phenocrysts (Wenzel et al., 2001; Fulignati et al., 2004; Dallai et al., 2011; Redi et al., 2017). Experimental olivines obtained during assimilation of 10 wt.% $CaCO_3$ show CaO contents up to ~1.5 wt.% (Fig. 1), resembling the natural concentration levels (~1.4 wt.% CaO) measured in primitive magmatic skarn environments. At 1,200 °C, the assimilation of 10 wt.% $CaCO_3$ expands the stability field of clinopyroxene (~8%), but this phenomenon is observed only for the most evolved $^{melt}Mg\#_{72}$ basalt (Table 1). At 1,150 °C, clinopyroxene dominates the phase assemblage (~12%) of the uncontaminated $^{melt}Mg\#_{72}$ basalt and its amount increases (~20%) with increasing $CaCO_3$. In contrast, $^{melt}Mg\#_{75}$ and $^{melt}Mg\#_{78}$ basalts segregate clinopyroxene (~5-15%) only under the effect of $CaCO_3$ assimilation, evidencing that olivine is the unique stable mineral in the undoped primitive magmas (Table 1). This means that, at the magma chamber-host rock interface, the cosaturation surface of olivine and clinopyroxene is strictly dependent on the physicochemical state of the system in terms of *T*, ^{melt}Mg#, and $CaCO_3$ content.

In the experimental charges doped with 20 wt.% $CaCO_3$, the modal abundance of clinopyroxene (9-20%) is much lower than that (~40-90%) observed in highly decarbonated natural environments where magmatic rocks are tephrites, phonotephrites, and foidites. Indeed, the oxidative capacity of CO_2 released during $CaCO_3$ decomposition at the skarn shells produces highly oxidized melts ($fO_2 \sim$ MH buffer) with silica-poor ($SiO_2 \approx 40$-46 wt.%), alkali-rich ($Na_2O+K_2O \approx 6$-11 wt.%) compositions (Fulignati et al., 2000, 2004; Gaeta et al., 2009; Mollo et al., 2010; Di Rocco et al., 2012; Gozzi et al., 2014; Mollo and Vona, 2014; Ammannati et al., 2016). The desilication reaction is greatly controlled by the fractionation of (Fe^{3+}-bearing) clinopyroxenes at temperatures of 800-1,150 °C, largely exceeding the thermal barrier (600 °C) for calcite breakdown (Lentz, 1999; Mollo et al., 2013a). Clinopyroxene-rich skarn shells (with minor or absent olivine) control the formation of highly decarbonated/oxidized rocks solidifying at low ($T \leq 1{,}150$ °C) thermal conditions (Gaeta et al., 2009; Mollo et al., 2010; Di Rocco et al., 2012). In contrast, the degree of clinopyroxene crystallization is much lower from less oxidized basaltic magmas equilibrated at 1,200-1,250 °C. As a consequence, there is not an effective competitor for CaO incorporation in olivine crystals and the concentration of alkali in the residual melt does not substantially increase due to the relative low olivine content. This phenomenon is typical of high temperature systems where primitive endoskarn-bearing dunite cumulates record mineralogical and textural evidences of mixing between olivine-saturated magmas and CaO-rich melts (Wenzel et al., 2001, 2002; Hayes et al., 2015).

From a compositional point of view, experimental data from this study evidence that Fo in olivine is positively correlated with *T*, ^{melt}Mg#, and $CaCO_3$, whereas Ca-ol is mostly controlled by the degree of $CaCO_3$ assimilation (Fig. 2). This geochemical variation can be expressed by the general reaction:

$$\left[2CaCO_3\right]^{cal} + \left[SiO_2 + 2MgO\right]^{melt} + \left[Fe_2SiO_4\right]^{Ol} = \\ \left[Mg_2SiO_4 - Ca_2SiO_4\right]^{Ol} + \left[2FeO\right]^{melt} + \left[2CO_2\right]^{fluid} \qquad (1)$$

Reaction (1) describes the high temperature, less oxidized (fO_2 ~ QFM buffer) domain that develops at the periphery of magma chambers when olivine-saturated basaltic magmas are initially contaminated by CaO-rich melts from the skarn shells. In this scenario, olivine occurs as a stable phase at the early stage of $CaCO_3$ assimilation, showing high-Fo, high-CaO, and low-NiO contents (Dallai et al., 2011; Ammannati et al., 2016). Notably, NiO in the experimental Fo_{87-93} olivines decreases from 0.65 to 0.15 wt.% with increasing $CaCO_3$, in agreement with that observed for natural phenocrysts (Fo_{86-93} and 0.09-0.53 wt.% NiO) from cumulate rocks (Wenzel et al., 2001, 2002; Gaeta et al., 2009; Dallai et al., 2011; Di Rocco et al., 2012; Ammannati et al., 2016). Ni basically occupies the small M1 crystallographic site of olivine (Annersten et al., 1982; Galoisy et al., 1995), responding to high crystal field effects (Wood, 1974). At magmatic temperatures, Fe^{2+} is preferentially ordered in the M2 site (Heinemann et al., 1999), whereas Mg is randomly distributed between M1 and M2 sites. Since Ca is essentially restricted to only the large M2 site, the effect of carbonate assimilation increases the number of Ca-Fe^{2+} substitutions (Coogan et al., 2005). The high CaO abundance in olivine (Fig. 1) is addressed to the strong codependency between Fo molecule and the mafic melt composition (Libourel, 1999). According to the equilibrium Fe-Mg exchange reaction (Roeder and Emslie, 1970), the Mg/Fe^{2+} ratio of olivine increases with increasing the MgO/FeO ratio of the melt, thus enhancing the Fo component (Fig. 2). At the same time, mixing phenomena between uncontaminated basalts and CaO-rich melts from the skarn shells lead to the formation of desilicated and decarbonated magmas. To better demonstrate this contamination mechanism, the activities of silica ($a^{melt}_{SiO_2}$), calcium (a^{melt}_{CaO}), and magnesium (a^{melt}_{MgO}) of the experimental melts have been calculated through the pseudo-activity models of Bottinga at al. (1981), Libourel (1999), and Leeman (1978), respectively:

$$a_{SiO_2}^{melt} = X_{SiO_2}^{melt} / \left(X_{SiO_2}^{melt} + X_{TiO_2}^{melt} + X_{Na_2O}^{melt} + X_{K_2O}^{melt} \right), \tag{2}$$

$$a_{CaO}^{melt} = \left(X_{CaO}^{melt} + X_{Na_2O}^{melt} + X_{K_2O}^{melt} \right)^2 / \left(X_{SiO_2}^{melt} + X_{TiO_2}^{melt} \right), \text{ and} \tag{3}$$

$$a_{MgO}^{melt} = X_{MgO}^{melt} / \left(X_{MgO}^{melt} + X_{FeO}^{melt} + X_{MnO}^{melt} + X_{CaO}^{melt} + X_{NiO}^{melt} \right) \tag{4}$$

Where X_i^{melt} is the molar fraction of the element *i* in the melt. Results from these calculations are plotted in the [(Fo+Ca-ol)/Fa] vs. [($a_{CaO}^{melt} + a_{MgO}^{melt}$)/$a_{SiO_2}^{melt}$)] diagram (Fig. 3) showing an appreciable positive correlation ($R^2 = 0.67$) between the olivine molecule proportions and the melt activity-composition relations. Note that the [($a_{CaO}^{melt} + a_{MgO}^{melt}$)/$a_{SiO_2}^{melt}$)] term acts as an indicator of open-system processes, accounting for either the CaO-rich, SiO_2-poor nature of the contaminated basalts, or the primitive character of the melt. According to the early formula proposed by Leeman (1978), [($a_{CaO}^{melt} + a_{MgO}^{melt}$)/$a_{SiO_2}^{melt}$)] should be intended as a complex activity function where the activities of SiO_2, CaO, and MgO are approximated according to equations (2), (3), and (4). The carbonate assimilation process is accompanied by an increase of a_{CaO}^{melt} and a decrease of $a_{SiO_2}^{melt}$ (Ferguson, 1978; Libourel, 1999). This facilitates the incorporation of Fo in olivine (Fig. 3) that, in turn, is governed by the activity of silica in the melt (Leeman, 1978). Note also that a_{MgO}^{melt} greatly enlarges the stability field of olivine (Roeder and Emslie, 1970; Ford et al., 1983; Snyder and Carmichael, 1992; Bedard, 2005). As a consequence olivine crystallization is ubiquitous in basaltic systems contaminated by $CaCO_3$ assimilation up to 20 wt.%, despite the stability field of olivine is reduced in favor of clinopyroxene (Table 1).

Previous experimental (Mollo et al., 2010; Jolis et al., 2013; Mollo and Vona, 2014; Carter and Dasgupta, 2015) and natural (Gaeta et al., 2009; Troll et al., 2012, 2013; Doroshkevich et al., 2012; Spandler et al., 2012; Del Bello et al., 2014) studies have documented that a high-calcium activity in magmas favors abundant clinopyroxene formation. The chemistry of clinopyroxene progressively changes from the magmatic domain towards the skarn shells, according to the following expression (Mollo et al., 2010; Mollo and Vona, 2014):

$$\begin{aligned}&[2CaCO_3]^{cal} + [2Al_2O_3 + TiO_2 + FeO]^{melt} + [CaMgSi_2O_6 - Mg_2Si_2O_6]^{Cpx} = \\ &[CaAlAlSiO_6 - CaFeAlSiO_6 - CaTiAlSiO_6]^{Cpx} + [3MgO + SiO_2]^{melt} + [2CO_2]^{fluid}\end{aligned} \qquad (5)$$

Results from this study conform to reaction (5), attesting that CaTs+CaFeTs+CaTiTs in clinopyroxene increase with $CaCO_3$ by lowering the amount of Di+En (Table 2S). Reactions (1) and (5) can be also combined to describe the spatial and temporal evolution of a basaltic system contaminated by carbonate material:

$$\begin{aligned}&[4CaCO_3]^{cal} + [2Al_2O_3 + TiO_2]^{melt} + [Fe_2SiO_4]^{Ol} + [CaMgSi_2O_6 - Mg_2Si_2O_6]^{Cpx} = \\ &[Mg_2SiO_4 - Ca_2SiO_4]^{Ol} + [CaAlAlSiO_6 - CaFeAlSiO_6 - CaTiAlSiO_6]^{Cpx} \\ &+ [MgO + FeO]^{melt} + [4CO_2]^{fluid}\end{aligned} \qquad (6)$$

The generalized decarbonation reaction (6) evidences that, as the degree of $CaCO_3$ assimilation increases, the contamination of magma proceeds from i) a high temperature, less oxidized domain characterized by olivine-saturated basaltic melts (Dunworth and Wilson, 1998; Wenzel et al., 2001, 2002; Hayes et al., 2015) to ii) an intermediate domain marked by olivine and clinopyroxene cosaturation (Fulignati et al., 2000, 2004; Dallai et al., 2011; Redi et al., 2017) to iii) a low temperature, highly oxidized domain governed by abundant clinopyroxene fractionation and formation of silica-poor, alkali-rich melts (Battistini et al., 2001; Gaeta et al., 2009; Di Rocco et al., 2012; Carter and Dasgupta, 2015). Therefore, reaction (6) requires that the iron speciation in the melt progressively changes under the oxidative action of CO_2, in agreement with the expression (e.g., Spandler et al., 2012):

$$[CO_2]^{fluid} + [2FeO]^{melt} = [CO]^{fluid} + [Fe_2O_3]^{melt} \quad (7)$$

In an open-system, the continuous flux of CO_2 gas through the magma shifts the equilibrium of reaction (7) to the right side, resulting in more oxidizing conditions (Connolly and Cesare, 1993). From the innermost part of the magma chamber towards the skarn shells, more oxidized magmas are produced through the redistribution of C–H–O species between melt and fluids. The progressive oxidation of magma during carbonate assimilation contributes to the destabilization of (Fe^{2+}-bearing) olivine and the crystallization of (Fe^{3+}-bearing) clinopyroxene (Wenzel et al., 2002; Gaeta et al., 2009; Del Bello et al., 2014; Mollo and Vona, 2014; Carter and Dasgupta, 2015). The stoichiometry of reaction (6) denotes as the number of MgO and FeO moles in the decarbonated magma increases through the coupled substitutions Fa ↔ Fo-Ca-ol and Di-En ↔ CaTs-CaFeTs-CaTiTs. Importantly, this exchange reaction explains also the crystallization of Al-Mg-rich spinel under more oxidized conditions (Fulignati et al., 2000, 2004; Wenzel et al., 2001, 2002; Gaeta et al., 2009; Di Rocco et al., 2012), in agreement with the CaO-rich melt inclusions found in olivine and spinel phenocrysts formed at the reaction-cumulate zone (Conte et al., 2009).

4.2. Divalent cation partitioning

Decarbonation experiments from this study provide a new dataset (Table 6S) of olivine-melt partition coefficients for Ni, Mg, Fe, Mn, and Ca applicable to primitive magmatic skarn environments. D_i^{2+} is calculated as C_i^{xls} / C_i^{melt}, where C_i^{xls} is the concentration of a chemical element *i* in the crystal and C_i^{melt} is the concentration of the same element in the melt. Despite the effects of temperature and bulk composition on D_i^{2+} are inextricably interrelated by phase relationships (e.g., Snyder and Carmichael, 1992; Libourel, 1999), D_{Ca}^{2+} and D_{Mg}^{2+} are observed to increase with increasing $CaCO_3$, whereas D_{Fe}^{2+}, D_{Mn}^{2+}, and D_{Ni}^{2+} decrease (Fig. 4). D_{Ca}^{2+}, D_{Mn}^{2+}, and D_{Ni}^{2+} are also positively correlated with ^{melt}Mg# (Fig. 4).

The $\ln D_i^{2+}$ vs. 1/T plot (Fig. 5a) is tentatively used to evaluate the individual effect of temperature on the partitioning behavior of divalent cations. The plot illustrates the decrease of the partition coefficient with increasing temperature (Fig. 5a), in agreement with the thermodynamic formalism describing the positive entropy of fusion of silicate minerals (Blundy and Wood, 1994; Wood and Blundy, 1997):

$$\ln D_i^{2+} = \ln\left(\gamma_i^{melt} / \gamma_i^{Ol}\right) + \left(\Delta G^{fusion} / RT\right) \tag{8}$$

Where γ_i^{melt} and γ_i^{Ol} are, respectively, the activity coefficients of the element i in the melt and olivine, ΔG^{fusion} is the Gibbs free energy of fusion (i.e., the difference between the free energy of melt and isochemical olivine at the temperature T of the system), and R is the universal ideal gas constant. The first term and the second term on the right of reaction (8) refer to the dependence of D_i^{2+} on the bulk composition and temperature, respectively. These terms can be parameterized through the regression analysis of experimentally-derived partition coefficients. For example, D_{Ni}^{2+} ($R^2 = 0.66$), D_{Mg}^{2+} ($R^2 = 0.86$), and D_{Fe}^{2+} ($R^2 = 0.68$) are moderately correlated with T (Fig. 5a), as cations with relatively small (≤ 0.78 Å) ionic radii and high ionic potentials (Hart and Davis, 1978; Leeman 1978; Takahashi, 1978; Wang and Gaetani, 2008). In contrast, D_{Mn}^{2+} ($R^2 = 0.21$) and D_{Ca}^{2+} ($R^2 = 0.41$) are weakly influenced by T (Fig. 5a), as cations with relatively large (≥ 0.83 Å) ionic radii and low ionic potentials (Henderson and Dale, 1968; Watson, 1977; Kohn and Schofield, 1994; Snyder and Carmichael, 1992; Libourel, 1999). Below 880 °C, Fe^{2+} tends to order onto the M1 site with increasing temperature, but it is also known that Fe^{2+} concentrates on the M2 site above 880 °C (Heinemann et al., 1999). Distortion of the M1 and M2 octahedra increases with substitution of the larger Fe^{2+} cation for Mg (Papike et al., 2005). According to the ionic size criteria, the large Ca (Coogan et al., 2005) and partially Mn (Francis and Ribbe, 1980; Henderson et al. 1996; Redfern et al. 1996) cations have no crystal field stabilization energy in olivine, entering into the larger and more distorted M2 site. The opposite occurs for Ni, being essentially restricted to the smaller Ml site (Annersten et al., 1982; Galoisy et al., 1995). During $CaCO_3$ assimilation, the number of Ca atoms available in the melt phase increases roughly two-fold and the bulk composition shifts from ~11 to ~22 wt.% CaO (Table 2S). As a consequence, Ca is greatly incorporated into the M2 site of olivine, responding to the effect of melt chemistry rather than temperature changes (cf. Libourel, 1999). Under such circumstances, a_{CaO}^{melt} is the most effective melt compositional parameter describing the variance of D_i^{2+} (Fig. 5b). This agrees with the studies of Watson (1979) and Jurewicz and Watson (1988), denoting as D_{Ca}^{2+} can be approximated as a linear function of Ca in the melt.

4.2.1. Ca partitioning

D_{Ca}^{2+} is documented to linearly increase with decreasing Fo in olivine (Jurewicz and Watson, 1988), following the apparent relationship determined by the colinearity between T and Fo (Libourel, 1999). Exchange reactions for minor divalent cations involve substitutions for both Fe^{2+} and Mg in the olivine crystal structure, as expressed by the formalism of Snyder and Carmichael (1992):

$$X_{Fa}^{Ol} FeSi_{1/2}O_2^{Ol} + X_{Fo}^{Ol} MgSi_{1/2}O_2^{Ol} + M^{2+}O^{melt} = X_{Fa}^{Ol} FeO^{melt} + X_{Fo}^{Ol} MgO^{melt} + M^{2+}Si_{1/2}O_2^{Ol} \qquad (9)$$

M^{2+} refers to Ca, whereas X_{Fa}^{Ol} and X_{Fo}^{Ol} indicate the mole fractions of $FeSi_{1/2}O_2^{Ol}$ and $MgSi_{1/2}O_2^{Ol}$ in olivine, respectively. The partitioning of Ca is related to a marked non-ideal substitution (Mukhopadhyay and Lindsley, 1983; Adams and Bishop, 1985), causing that the equilibrium constant of reaction (9) has both compositional and temperature dependence. From the definition of the Gibbs free energy, reaction (9) can be rearranged to quantitatively evaluate these relative contributions on D_{Ca}^{2+} (Snyder and Carmichael, 1992):

$$\ln D_{Ca}^{2+} = -11.32\ (\pm 1.25) + 12{,}468\ (\pm 2{,}332)/T(K) - 0.3478\ (\pm 0.255)\left[X_{Fo}^{Ol} \ln\left(X_{MgO}^{melt}/a_{Fo}^{Ol}\right) + X_{Fa}^{Ol} \ln\left(X_{FeO}^{melt}/a_{Fa}^{Ol}\right)\right] \quad (10)$$

Where a_{Fo}^{Ol} and a_{Fa}^{Ol} are the activity of Fo and Fa in olivine, respectively. When equation (10) is tested with experimental data from this study, the predicted D_{Ca}^{2+} values are affected by a very low uncertainty of $^{\text{Eqn.(10)}}$SEE = 0.02 (Fig. 1aS). The success of equation (10) with data not included in its calibration dataset highlights as models based on thermodynamic principles can be realistically extrapolated to a broad range of compositions outside of the experimental database used to formulate the activity coefficients of divalent cations (c.f. Toplis, 2005). Moreover, olivine and melt compositions from decarbonation experiments allow to isolate the effect of *T* from that of CaO produced via $CaCO_3$ assimilation. When the temperature of the system is kept constant, Ca cations into M2 crystallographic site increases with increasing CaO in the melt, causing that the number of structural sites available for Fe decreases (Fig. 1). In other words, when the influence of *T* is isolated, both Ca and Fo content in olivine increases as the melt phase becomes progressively enriched in CaO (Figs. 1 and 2). The cation-oxygen bond distance in olivine decreases from 2.17 (Fa) to 2.11 Å (Fo), implying that the incorporation of large divalent cations into crystal structure is more facilitated for Fo-rich olivines (Snyder and Carmichael, 1992 and references therein). Coherently, experimental $Fo_{87\text{-}92}$ olivines from this study are consistent with those obtained by Jurewicz and Watson (1988), showing that D_{Ca}^{2+} is a linear function of Fo content in olivine. According to Berndt et al. (2005), Fo in olivine also increases with $^{\text{melt}}$Mg# over a wide range of basaltic compositions, temperature, and oxygen fugacities. Experiments from this study extend this finding to decarbonated melts, showing positive correlations between Fo, ^{melt}Mg#, and D_{Ca}^{2+} (Fig. 2). However, Toplis and Carroll (1995) have observed that the linear dependence of D_{Ca}^{2+} on Fo ceases for crystals with forsterite content lower than 55 mol%. This occurs because the activity-composition relations in olivine vary significantly over broad chemical intervals, reflecting deviation from ideality in the forsterite-fayalite solid solution (Toplis, 2005). The close relationship between D_{Ca}^{2+} and silicate melts has been the focus of several previous works (Libourel et al., 1989; Shi and Libourel, 1991; Shi, 1993; Libourel, 1999), showing that calcium and silica in the melt phase are colinear compositional variables determining the enrichment of Ca cations in olivine. In this framework, the calcium pseudo-activity model proposed by Libourel (1999) represents a well-calibrated proxy to predict the partitioning of calcium between olivine and silicate melts reproducing a wide spectrum of natural magmatic compositions (cf. Roeder, 1974; Longhi et al., 1978; Dunn, 1987; Colson et al., 1988; Gee and Sack, 1988; Longhi and Pan, 1988; Nielsen et al., 1988; Snyder et al., 1993; Toplis and Carroll, 1995). According to this model, the effect of melt composition on Ca partitioning is described by the relationship:

$$D_{Ca}^{2+} = \left[CaO / \left(CaO + MgO\right)\right]^{Ol} / a_{CaO}^{melt} \tag{11}$$

It is worth noting that silicate melts from primitive magmatic skarn environments are subjected to important chemical modifications due to the anticorrelated effects of CaO enrichments and SiO_2 depletions (Wenzel et al., 2001, 2002). Therefore, olivine-melt compositional changes caused by the assimilation of carbonate material (i.e., open-system process) are not compatible with the CaO concentration levels of natural magmas (i.e., closed-system process). This causes that equation (11) is affected by a systematic overestimate ($^{Eqn.(11)}$SEE = 0.20) for primitive magmatic skarn compositions (Fig. 1bS). The ability prediction of equation (11) can be significantly improved

($^{Eqn.(12)}$SEE = 0.01 and $^{Eqn.(12)}$R^2 = 0.76) by simplifying the pseudo-activity parameter as follows (Fig. 1cS):

$$a_{CaO}^{melt} = X_{CaO}^{melt} / X_{SiO\ 2}^{melt} \tag{12}$$

This result is not surprising because, according to Libourel (1999), the amount of Ca entering olivine is proportional to the number of Si and Ca atoms available in the melt structure in the form of network-former (i.e., Si-O-Si) and network-modifier (i.e., Ca-O-Si), respectively. As the melt becomes less polymerized, the number of bridging oxygens (i.e., BO, oxygens bonded to two tetrahedrally coordinated cations) decreases, whereas the amount of non-bridging oxygens (i.e., NBO, oxygens bonded to a tetrahedrally coordinated cation and to a different cation in another coordination state) increases (Kohn and Schofield, 1994; Lee and Stebbins, 2003). The melt structure is expressed as NBO/T (i.e., the number of NBO per tetrahedrally coordinated cations T; Mysen et al., 1985), whereas the different Si network connectivity in the melt is described in terms of Q^n-species (i.e., individual structure of oxygen tetrahedra surrounding a central, tetrahedrally-coordinated cation; Mysen et al., 1982). The distribution of Q^n-species in silicate melts is governed by the equilibrium reaction: $2Q^n = Q^{n-1}+Q^{n+1}$. The reaction shifts to the right as the ionic potential (Z^+/r_i^2 where Z^+ and r_i are cation charge and radius, respectively) of the network modifying cations increases (Maekawa et al., 1991). This explains why, as network modifiers, divalent alkaline earth metals (Z^+/r_i^2 >2) have a more effective role in the melt structure than monovalent alkaline metals (Z^+/r_i^2<< 2). Cation stabilization in a polyhedron of oxygens is proportional to Z^+/r_i^2 (Watson, 1976) and, consequently, alkaline earth metals are likely also more soluble into the low-SiO_2 melt (basic melt) than high-SiO_2 melt (acidic melt). As the concentration of Ca-O-Si bonds increases during carbonate assimilation, the melt polymerization decreases according to the cation exchange (Libourel, 1999):

Si-O-Si + Ca-O-Ca ↔ 2Ca-O-Si (13)

It is apparent that a_{CaO}^{melt} has a non-ideal behavior in multicomponent silicate melts, showing a non-linear correlation with X_{CaO}^{melt} (Rein and Chipman, 1965). However, the significant improvement obtained by equation (12) indicates that the formation of Ca-O-Si bonds is energetically more favored in magmas assimilating great amounts of carbonate material. The increase of Ca cations in the melt results in i) an increase in the proportion of octahedral relative to tetrahedral sites and ii) changes of the energy of substitution of Ca in octahedral sites (cf. Leeman, 1978). Therefore, in primitive magmatic skarn systems, the combined effects of decarbonation and desilication cause that SiO_2-poor, CaO-rich melts coexist with Ca-rich olivines. In this specific scenario, the variation of D_{Ca}^{2+} can be mostly modeled as function of the number of Si and Ca atoms available in the melt structure, independently of the influence of *T* and Fo content.

4.2.2. Mg partitioning

Considering the temperature-composition relationship that governs the partitioning behavior of chemical elements, different solution of the thermodynamic equation (8) have been proposed by authors (e.g., Roeder and Emslie, 1970; Langmuir and Hanson, 1981; Ford et al., 1983; Beattie, 1993; Putirka et al., 2005, 2007; Putirka, 2008; Jones, 2016; Pu et al., 2017) to derive models predicting either D_{Mg}^{2+} or the saturation *T* of olivine. Through the statistical formula for the standardized regression coefficient (i.e., the original unstandardized regression coefficient of the independent variable, multiplied by the standard deviation of the independent variable, and divided by the standard deviation of the dependent variable), it is possible to quantify the influence of *T*, a_{CaO}^{melt} (i.e., the degree of carbonate assimilation) and MgO in the melt (i.e., the primitive character of the melt) on D_{Mg}^{2+}. Experimental data from this study show that D_{Mg}^{2+} increases by ~29% with increasing $CaCO_3$, and decreases by ~27% and ~44% with increasing T and X_{MgO}^{melt}, respectively. The amount of MgO in the melt is the parameter with the greatest influence on D_{Mg}^{2+}, coherently with the studies of Leeman (1978) and Kohn and Schofield (1994). However, D_{Mg}^{2+} is not (almost) univocally controlled by the isolated effect of MgO in the melt. In the recent review study of Pu et al. (2017), the olivine-melt equations of Beattie (1993) and Putirka et al. (2007) have been recognized as the most accurate predictive models for D_{Mg}^{2+}. Pu et al. (2017) have also reappraised the general formulation of Beattie (1993) to derive a new empirical model based on the regression fit of 123 olivine-melt experiments. To test the validity of all these models under open-system decarbonation conditions, the following equations from Beattie (1993) (i.e., equation 14), Putirka et al. (2007) (i.e., equation 15), and Pu et al. (2017) (i.e., equation 16) have been considered:

$$\begin{aligned} D_{Mg}^{2+} = &\left(0.666 - \left(0.0135 X_{CaO}^{melt} - 0.049 X_{MnO}^{melt} + 0.031 X_{FeO}^{melt}\right)\right) \\ &/\left(X_{MgO}^{melt} + 0.259 X_{MnO}^{melt} + 0.279 X_{FeO}^{melt} + 0.0056 X_{CaO}^{melt}\right) \end{aligned} \tag{14}$$

$$\begin{aligned} \ln D_{Mg}^{2+} = &-2.158 + 55.09 P(GPa)/T(°C) - 6.213 \cdot 10^{-2} X_{H2O}^{melt} \\ &+ 4{,}430 / T(°C) + 5.115 \cdot 10^{-2}\left(X_{Na2O}^{melt} + X_{K2O}^{melt}\right) \end{aligned} \tag{15}$$

$$\begin{aligned} \ln D_{Mg}^{2+} = &-4.74(\pm 0.2) + 6{,}701(\pm 182)/T(K) - 1.12(\pm 0.08)\ln\left(X_{FeO}^{melt} + X_{MgO}^{melt} + X_{MnO}^{melt} + X_{CaO}^{melt} + X_{NiO}^{melt}\right) \\ &- 1.08(\pm 0.15)\ln\left(X_{SiO2}^{melt}\right) + 0.64(\pm 0.07)\left[3.5\ln\left(1 - X_{Al2O3}^{melt}\right) + 7\ln\left(1 - X_{TiO2}^{melt}\right)\right] \end{aligned} \tag{16}$$

The comparison between predicted and experimentally-derived D_{Mg}^{2+} values provides that $^{Eqn.(14)}SEE$, $^{Eqn.(15)}SEE$, and $^{Eqn.(16)}SEE$ are 1.73 (Fig. 2aS), 0.96 (Fig. 2bS), and 1.27 (Fig. 2cS), respectively. Equation (14) of Beattie (1993) and equation (16) of Pu et al. (2017) include regression parameters for the melt (i.e., X_{Ca}^{melt} and X_{SiO2}^{melt}) that are greatly influenced by magma decarbonation and desilication phenomena, thus lowering their ability predictions under open-system conditions. Mg is undoubtedly the major component of magmatic olivines and, as evidenced by the decarbonation reaction (6), its concentration increases with Ca content. For the case of Colli Albani Volcanic Complex (Italy), natural olivines from endoskarns are systematically enriched in Fo and CaO with respect to those from uncontaminated magmas (Gaeta et al., 2009; Di Rocco et al., 2014). The same geochemical trend has been observed for xenoliths from several eruptions of Vesuvius (Italy; Dallai et al., 2011; Hayes et al., 2015; Jolis et al., 2015; Redi et al., 2017) and dunite cumulates from the Ioko-Dovyren Intrusion (North Baikal, Russia; Wenzel et al., 2001, 2002). On this basis, the values of D_{Mg}^{2+} experimentally-derived from this study can be parameterized as a function of a_{CaO}^{melt}, *T*, and X_{MgO}^{melt}, as follows (cf. Putirka et al., 2007):

$$\begin{aligned}\ln D_{Mg}^{2+} = {} & 0.03\,(\pm 0.02)\,a_{CaO}^{melt} + 0.110\,(\pm 0.03)\cdot 10^{4}/T(K) \\ & - 6.97\,(\pm 0.42)\,X_{MgO}^{melt} + 1.93\,(\pm 0.23)\end{aligned} \tag{17}$$

Within the temperature-composition space of carbonate-bearing basaltic magmas (Fig. 2dS), D_{Mg}^{2+} variations are successfully described by equation (17), providing good regression statistics of $^{\text{Eqn.(17)}}R^2 = 0.99$ and $^{\text{Eqn.(17)}}\text{SEE} = 0.01$.

4.2.3. Fe partitioning

Thermodynamic modeling of olivine-basalt compositions have evidenced that the partitioning of Fe^{2+} is linearly dependent of D_{Mg}^{2+}, but independent of *P* and *T* (Jones, 1984, 2016). According to the observation that i) the stoichiometry of olivine is relatively simple, ii) Mg and Fe^{2+} totally dominate all other divalent cations, and iii) the partitioning of transition metals is greatly controlled by heats of fusion rather than heats of mixing for ideal melt and crystal solutions, Jones

(2016) (i.e., equation 18) and Wang and Gaetani (2008) (i.e., equation 19) proposed the following regression fits:

$$D_{Fe}^{2+}(\pm 0.13) = 0.298\, D_{Mg}^{2+} + 0.027 \qquad (18)$$

$$\ln D_{Fe}^{2+} = 1.15(\pm 0.04)\ln D_{Mg}^{2+} + 0.64(\pm 0.06) \qquad (19)$$

The application of these linear models to olivine-melt pairs from uncontaminated basaltic experiments yields errors ($^{\text{Eqn.(18)}}$SEE = 0.23 and $^{\text{Eqn.(19)}}$SEE = 0.10) that are quite similar to the intrinsic calibration errors calculated by Jones (2016) and Wang and Gaetani (2008). In contrast, equations (18) and (19) show systematic overestimates ($^{\text{Eqn.(18)}}$SEE = 0.52 and $^{\text{Eqn.(19)}}$SEE = 0.30) for olivine-melt pairs from decarbonation experiments (Figs. 3a-bS). It is interesting to note that D_{Fe}^{2+} varies approximately by ~14%, ~37%, and ~49% as a function of T, X_{MgO}^{melt}, and $CaCO_3$, respectively. According to reaction (10), the thermodynamics of olivine mixing requires that Ca substitutes for both Fe^{2+} and Mg in the crystal lattice during magma-carbonate interaction. This is consistent with the study of Jurewicz and Watson (1988) attesting that the concentration of calcium in olivine is highly correlated with iron in both crystal and melt. Due to differences between Fe^{2+} and Mg cation radii, the Ca-Fe^{2+} substitutions in olivine are more facilitated than Ca-Mg ones, as the amount of Ca cations in the melt increases (Warner and Luth, 1973; Adams and Bishop, 1985). In this view, the equation (18) of Jones (2016) can be refined by considering the influence of the activity of calcium in the melt:

$$D_{Fe}^{2+} = 0.11(\pm 0.01) - 0.46(\pm 0.04)D_{Mg}^{2+} - 0.13(\pm 0.05)a_{CaO}^{melt} \qquad (20)$$

The regression fit of equation (20) is greatly improved ($^{\mathrm{Eqn.(20)}}R^2 = 0.92$ and $^{\mathrm{Eqn.(20)}}SEE = 0.03$; Fig. 3cS), pointing out that the linear relationship between D_{Fe}^{2+} and D_{Mg}^{2+} cannot be assumed as independent on melt composition under open-system conditions. According to the exchange reaction (13), the melt polymerization decreases as the concentration of Ca-O-Si bonds increases (Shi and Libourel, 1991; Libourel, 1999), thus influencing the proportion of octahedral relative to tetrahedral sites and, ultimately, the activity of the chemical species in the melt (Mysen, 2004). The increasing amount of Ca cations in the melt enhances the breaking of Si−O−Si bonds and reduces the number of NBO necessary for the network-modifying cations to form their preferred coordination polyhedra. In other words, the disruption of tetrahedral units by Ca cations increases the number of structural sites critically important to accommodating network-modifying cations in the melt structure (i.e., Fe^{2+}, Mn, and Ni), lowering the value of D_i^{2+}. Several experimental studies (e.g., Mysen and Virgo, 1980; Mysen et al., 1982; Kushiro and Mysen, 2002; Gaetani, 2004; Mysen, 2004; Mysen and Dubinsky, 2004; Li and Ripley, 2010; Wang and Gaetani, 2008) have demonstrated that D_i^{2+} for network-modifying cations varies as a function of NBO/T. The solubility of network-modifying cations in silicate melts decreases as the activity of NBO decreases with increasing silica content (Mysen, 2004), so that divalent cations are preferentially incorporated into olivine crystal lattice (e.g., Libourel, 1999). Log-linear relations between D_i^{2+} and NBO/T exhibit more negative slopes with increasing the valence cation due to an increased availability of NBO to form the metal-oxygen polyhedra (Walter and Thibault, 1995; Jana and Walker, 1997; Jaeger and Drake, 2000). More specifically, steric hindrance leads to the cation with the highest ionic potential (Ni >Mg >Fe^{2+} >Mn >Ca) to form bonds with oxygen in the less polymerized Q^n-species (Mysen and Dubinsky, 2004). Following these principles, Wang and Gaetani (2008) rearranged the thermodynamically-based equation of Beattie et al. (1991) in the form:

$$\ln D_{Fe}^{2+} = -0.51(\pm 0.02)\ln(NBO/T) + 6{,}000(\pm 400)/T(K) - 3.8(\pm 0.4) \tag{21}$$

Noteworthy, the values of D_{Fe}^{2+} predicted by equation (21) match quite well ($^{\mathrm{Eqn.(21)}}$SEE = 0.25) with those measured from magma-carbonate interaction experiments (Fig. 3dS). According to Wang and Gaetani (2008), the partitioning of Fe^{2+} decreases with melt depolymerization (i.e., with $CaCO_3$ assimilation; Fig. 3dS) due to the enhanced disorder in the melt structure and the reduced occupancy of octahedral sites by divalent cations (Leeman, 1978). These latter are bonded to energetically non-equivalent NBO, so that the bond strength between Si and NBO depends on the number of BO in the different Q^n-species (Mysen, 2004). Therefore, D_{Fe}^{2+} in the equation (21) is non-linear function of NBO/T because of the different i) solution mechanisms of network-modifying cations, ii) activity–composition relations of chemical elements in decarbonated melts, and iii) types of NBO available in the coexisting Q^n-species (Mysen, 2004).

4.2.4. Mn partitioning

Since the study of Watson (1977), silicate melts have been considered as complex atomic structures that, together with the saturation temperature of olivine, govern the partitioning behaviour of Mn. However, D_{Mn}^{2+} is more dependent on melt composition and structure rather than temperature (Watson, 1977). The same conclusion was reached by Kohn and Schofield (1994) for the simplified Fo-Ab-An system in which small changes in NBO/T are accompanied by large D_{Mn}^{2+} variations in highly depolymerized melts, but the effect of changing temperature by 100 °C is too small to be observable. Wang and Gaetani (2008) proposed a thermodynamically-based expression to quantify D_{Mn}^{2+} as a function of both melt composition and temperature:

$$\ln D_{Mn}^{2+} = -0.41\,(\pm 0.06)\ln(NBO/T) + 6{,}100\,(\pm 1{,}500)/T(K) - 4.0(\pm 0.9) \tag{22}$$

Equation (22) is applicable to a relatively broad range of melt compositions in equilibrium with primitive olivines that, importantly, are compositionally similar to those (Fo_{87-93}) from this study. However, D_{Mn}^{2+} values predicted by equation (22) are underestimated ($^{Eqn.(22)}$SEE = 0.54) relative to those measured for olivine-melt pairs from decarbonation experiments (Fig. 4aS). D_{Mn}^{2+} progressively decreases with increasing $CaCO_3$ due to the lower chemical potential of Mn, as the number of NBO increases in the more depolymerized melt (Fig. 4aS). Note that steric hindrance effects are more operative in CaO-rich melts, making not possible to satisfy the bonding requirements for Mn without distorting and destabilizing the silicate framework (Kohn and Schofield, 1994). Although the magnitude of the partition coefficient scales with the degree of melt polymerization, the melt structure affects significantly the element partitioning when NBO/T is lower than a certain threshold value. For example, complementary results from Gaetani (2004), Huang et al. (2006), and Mollo et al. (2016) denote that the partitioning of REE between clinopyroxene and silicate melt increases markedly below a NBO/T equals to 0.4. Turning to the case of olivine, Schmidt et al. (2006) and Wang and Gaetani (2008) reported that the dependence of divalent cation partitioning on melt composition becomes negligible at NBO/T >0.6. The review study of Bédard (2005) reports a compilation of olivine-melt partition coefficients from both experimental and natural products analyzed over a span of 25 years. The D_{Mn}^{2+} vs. NBO/T diagram (Fig. 6) shows a monotonic increase of the partition coefficients from ~0.4 to ~4.1, as NBO/T decreases from ~1.8 to ~0.3. D_{Mn}^{2+} values from decarbonation experiments are consistent with those from Bédard (2005), aligning along a trend with a steeper slope at NBO/T <0.6 (Fig. 6). At higher NBO/T, the polymeric units become completely dissociated and the number of BO decreases (Fig. 6). The change of D_{Mn}^{2+} reflects the combined effects of temperature, crystal chemistry, and melt structure (e.g., Bédard, 2005; Wang and Gaetani, 2008). In fact, if the number of Ca cations in the melt affects the activity of Mn (Kohn and Schofield, 1994), it is also true that an increasing $CaMgSiO_4$ component in olivine changes the standard free energy of Mn in the crystal lattice

(Takahashi, 1978). Mn and Ca cations reside in the same M2 crystallographic site and, therefore, the presence of one will to some degree affects the incorporation of the other, causing that D_{Mn}^{2+} decreases with increasing Ca into olivine (Lumpkin et al., 1983; Annersten et al., 1984; Akamatsu et al., 1988; Snyder and Carmichael, 1992). On this basis, the equation (22) of Wang and Gaetani (2008) can be refined for decarbonated magmas by including the X_{Ca}^{Ol} term:

$$\begin{aligned}\ln D_{Mn}^{2+} &= -0.41(\pm 0.11)\ln(NBO/T) + 65.39(\pm 25.18)/T(K) \\ &\quad - 0.42(\pm 0.07)X_{CaO}^{Ol} + 0.41(\pm 0.07)\end{aligned} \qquad (23)$$

As a result, the regression statistics ($^{\text{Eqn.(23)}}R^2 = 0.92$ and $^{\text{Eqn.(23)}}SEE = 0.03$) of equation (23) are remarkably improved. Therefore, for primitive magmatic skarn melts with NBO/T >0.6, Mn partitioning systematics can be more precisely quantified taking into account the control of both crystal and melt compositions (Fig. 4bS).

4.2.5. Ni partitioning

The temperature dependence of Ni-Mg exchange reaction is strictly related to the difference in the enthalpy of fusion between Mg_2SiO_4 and Ni_2SiO_4 components in olivine (Jones, 2016). At a given bulk composition, D_{Ni}^{2+} is observed to decrease with *P* and *T* (Matzen et al., 2013, 2017; Ammannati et al., 2016). On the contrary, during magma cooling and crystallization, most of D_{Ni}^{2+} changes are the effect of covarying temperature and melt composition (Watson, 1977; Hart and Davis, 1978; Lynn et al., 2017). Since Ca and Ni are strongly ordered and reside in different olivine crystallographic sites, D_{Ni}^{2+} and D_{Ca}^{2+} are found to be independent of X_{CaO}^{Ol} and X_{NiO}^{Ol}, respectively. According to the exchange equation (10), Snyder and Carmichael (1992) modeled the variation of D_{Ni}^{2+} through the thermodynamic solution:

$$\ln D_{Ni}^{2+} = -2.575\ (\pm 0.484)\ +\ 4{,}592\ (\pm 724)\ /\ T(K)\left[X_{Fo}^{Ol}\ \ln\left(X_{MgO}^{melt}\ /\ a_{Fo}^{Ol}\right) + X_{Fa}^{Ol}\ \ln\left(X_{FeO}^{melt}\ /\ a_{Fa}^{Ol}\right)\right] \tag{24}$$

Decarbonated data from this study are not adequately described ($^{\text{Eqn.(24)}}$SEE = 3.62; Fig. 5aS) by equation (24), suggesting that D_{Ni}^{2+} cannot be univocally addressed to the temperature-dependence exchange between Ni and Mg (cf. Snyder and Carmichael, 1992). For example, the broad range of Ni contents measured in natural olivines is caused by the marked variations of MgO and SiO_2 in the melt during crystallization (e.g., Irvine and Kushiro, 1976; Hart and Davis, 1978; Takahashi, 1978; Jones, 1984; Clague et al., 1991; Korenaga and Kelemen, 2000; Sobolev et al., 2005, 2007; Putirka et al., 2011; Matzen et al., 2013; Ammannati et al., 2016; Lynn et al., 2017). Moreover, among all divalent cations, Ni has the highest crystal field stabilization energy in octahedral sites (~29.2 kcal/mol; Dunitz and Orgel, 1957). Consequently, as the value of NBO/T decreases (i.e., the number of NBO to form coordination polyhedra decreases), Ni is preferentially incorporated into olivine crystal lattice relative to Mg (Henderson and Dale, 1968; Irvine and Kushiro, 1976; Watson, 1977; Takahashi, 1978). The variation of D_{Ni}^{2+} with NBO/T has been modeled by Wang and Gaetani (2008) through the expression:

$$\ln D_{Ni}^{2+} = -0.71\,(\pm 0.04)\,\ln(NBO\ /\ T)\ +\ 7{,}100\ (\pm 900)\ /\ T(K)\ -\ 2.5(\pm 0.6) \tag{25}$$

Although equation (25) has been calibrated specifically to siliceous eclogite partial melts or basalts, its predictive power ($^{\text{Eqn.(25)}}$SEE = 1.86; Fig. 5bS) for decarbonated compositions is apparently better than that of the activity-based equation (24). Noteworthy, Ca cations form NBO bonds less sterically hindered and energetically more favored than divalent cations with smaller ionic radii and higher ionic potentials, such as Ni (e.g., Kohn and Schofield, 1994; Mysen and Dubinsky, 2004; Mysen and Richet, 2005). Therefore, during $CaCO_3$ assimilation, the depolymerizing effect of Ca reduces the steric distortion of Ni octahedra in the melt (cf. Keppler, 1992; Keppler and

Bagdassarov, 1999; Mysen and Dubinsky, 2004; Jackson et al., 2005; Mysen, 2006, 2008; Wang and Gaetani, 2008; Li and Ripley, 2010) by enhancing cation solubility and lowering D_{Ni}^{2+} (Takahashi, 1978; Mysen and Virgo, 1980; Libourel, 1999; Schmidt et al., 2006; Mysen, 2007, 2008; Wang and Gaetani, 2008). In the review study of Pu et al. (2017), a set of melt components is used to describe the degree of depolymerization (also in agreement with the early studies of Beattie et al., 1991 and Beattie, 1993), in order to derive the following model for D_{Ni}^{2+}:

$$\begin{aligned}\ln D_{Ni}^{2+} = &-4.32\,(\pm 0.33) + 9{,}416\,(\pm 296)/T(K) - 0.71\,(\pm 0.13) \\ &\ln(X_{FeO}^{melt} + X_{MgO}^{melt} + X_{MnO}^{melt} + X_{CaO}^{melt} + X_{NiO}^{melt}) + 0.53\,(\pm 0.24) \\ &\ln(X_{SiO_2}^{melt}) + 0.35\,(\pm 0.11)\left[3.5\ln(1 - X_{Al_2O_3}^{melt}) + 7\ln(1 - X_{TiO_2}^{melt})\right]\end{aligned} \tag{26}$$

It is interesting to note that the parameterization of equation (26) makes the model very suitable for basaltic melts assimilating carbonate material, yielding $^{\mathrm{Eqn.(26)}}$SEE = 1.54 (Fig. 5cS). This outcome is a clear evidence that the partitioning behavior of Ni is independent of olivine chemistry, as the direct consequence of the control exerted by melt composition and structure on cations with a high ionic potentials (Gaetani 2004; Schmidt et al. 2006; Wang and Gaetani, 2008).

4.3. Cation exchange reactions

Cation redistribution reactions based on the equilibrium between olivine and melt are generally expressed by the exchange partition coefficient, $K_{D(i-j)} = \left(X_i^{Ol}/X_j^{Ol}\right)/\left(X_i^{melt}/X_j^{melt}\right)$, where *i* and *j* refer to the two chemical elements of interest. Roeder and Emslie (1970) argued that, under equilibrium conditions, $K_{D(Fe-Mg)}$ exhibits an approximately constant mean value of 0.30 (±0.03), irrespective of temperature, melt redox state, and bulk composition. Although this approach is used as an evidence of equilibrium in both natural and experimental systems, it is also know that $K_{D(Fe-Mg)}$ changes systematically from 0.13 to 0.45, responding to the variable physicochemical state of the crystallizing system (e.g., Longhi et al., 1978; Takahashi, 1978; Ford et al., 1983; Jones, 1984; Gee and Sack 1988; Herzberg and O'Hara 1998; Kushiro and Walter, 1998; Kushiro and Mysen, 2002; Toplis 2005; Mibe et al., 2006; Filiberto and Dasgupta, 2011; Putirka, 2016; Mollo and Hammer, 2017). The melt composition and structure have a great influence on the Fe^{2+}-Mg exchange, especially for the effect of Na_2O+K_2O (e.g., Sack et al., 1987; Gee and Sack, 1988; Toplis, 2005), TiO_2 (e.g., Jones, 1988; Wagner and Grove, 1997), SiO_2 (e.g., Longhi et al., 1978; Toplis, 2005), and NBO/T (e.g., Kushiro and Walter, 1998; Kushiro and Mysen, 2002; Mibe et al., 2006; Filiberto and Dasgupta, 2011). Bearing this in mind, Putirka (2016) has recently performed the global regression analysis of 1,270 experimental data from literature, finding that olivine crystals in equilibrium with both terrestrial and extraterrestrial magmas provide a mean Fe^{2+}-Mg exchange value of 0.33 (±0.04). In this respect, magma-carbonate interaction data from this study show that $K_{D(Fe-Mg)}$ narrowly changes from 0.29 to 0.36 (Table 7S), as a clear evidence of equilibrium crystallization of olivines from the decarbonated melts (cf. Bickle et al., 1977; Filiberto and Dasgupta, 2011; Matzen et al., 2011; Barr and Grove, 2013). As a further test of equilibrium, the measured $K_{D(Fe-Mg)}$ values have been compared with those predicted by the models of Toplis (2005) (i.e., equation 27) and Putirka (2016) (i.e., equations 28 and 29):

$$
\begin{aligned}
K_{D(Fe-Mg)} = \exp \Bigg\{ & \left[\frac{-6766}{RT(K)} - \frac{7.34}{R} \right] + \ln \left[0.036 \ \% \ X_{SiO_2}^{melt} \# - 0.22 \right] \\
& + \left[\frac{3{,}000 \left(1 - 2X_{Fo}^{Ol} \right)}{RT(K)} \right] + \left[\frac{0.035 \left(P(bar) - 1 \right)}{RT(K)} \right] \Bigg\}
\end{aligned} \tag{27}
$$

$$
K_{D(Fe-Mg)} = 0.25 + 0.0018 \, SiO_2 - 3.27 \cdot 10^{-4} \left(Na_2O + K_2O \right)^2 \tag{28}
$$

$$
\begin{aligned}
K_{D(Fe-Mg)} = & \ 0.0583 + 0.00252 \, SiO_2 + 0.028 \, P(GPa) \\
& - 0.0091 \left(Na_2O + K_2O \right) - 0.013383 \, \log(fO_2)
\end{aligned} \tag{29}
$$

The $\% X_{SiO_2}^{melt}\#$ parameter of equation (27) refers to the molar silica content of the melt recalculated according to Toplis (2005). Notably, the equation (29) of Putirka (2016) treats all iron in the melt as FeO_t, referring to a mean equilibrium value of Fe^{2+}-Mg exchange close to 0.29 (±0.051). For the present decarbonation experiments, equations (27), (28), and (29) evidence equilibrium olivine crystallization, yielding $K_{D(Fe-Mg)}$ values of 0.26-0.30, 0.32-0.34, and 0.23-0.27, respectively (Fig. 6S). The standard error of estimates ($^{Eqn.(27)}$SEE = 0.04, $^{Eqn.(28)}$SEE = 0.02, and $^{Eqn.(29)}$SEE = 0.02) are also very similar to the intrinsic calibration errors ($^{Eqn.(27)}$SEE = 0.03, $^{Eqn.(28)}$SEE = 0.04, and $^{Eqn.(29)}$SEE = 0.04) of the models. With increasing $CaCO_3$ assimilation, D_{Fe}^{2+} decreases from ~5% to ~13%, whereas D_{Mg}^{2+} increases from ~3% to ~5% (Fig. 4). The maximum deviation between D_{Fe}^{2+} and D_{Mg}^{2+} is calculated for basalts doped with 20 wt.% $CaCO_3$. However, $CaCO_3$ assimilation does not affect significantly the $D_{Fe}^{2+} / D_{Mg}^{2+}$ ratio, implying that the value of $K_{D(Fe-Mg)}$ increases only slightly. It is therefore concluded that the Fe^{2+}-Mg exchange reaction between olivine and decarbonated melt is not perfectly invariant with $K_{D(Fe-Mg)}$ ranging from 0.29 to 0.35, but the mean value of $K_{D(Fe-Mg)}$ equally tends towards the equilibrium condition of 0.33±0.04 established for terrestrial and extraterrestrial magmas (cf. Putirka, 2016).

According to Mysen (2008), the exchange reaction between Fe^{2+}/Ca/Mn/Ni and Mg quantitatively describes the equilibrium state of two cations with different electronic properties (e.g., ionic potentials) and different affinities for energetically non-equivalent NBO in Q^n-species. Fig. 7 shows that these exchange partition coefficients do not vary significantly with T and ^{melt}Mg#, responding to a restricted NBO/T change with maximum deviation of only ~16% (see also Table 7S). In contrast, important NBO/T changes are observed with increasing $CaCO_3$ (Fig. 7), showing maximum deviation of ~64%. The role of the melt structure has been broadly emphasized in literature as one of the most striking parameter determining $K_{D(Fe-Mg)}$ fluctuations (e.g., Kushiro and Walter, 1998; Kushiro and Mysen, 2002; Toplis, 2005; Mibe et al., 2006; Filiberto and Dasgupta, 2011). During cation partitioning between olivine and mafic melts, $K_{D(Fe-Mg)}$ increases with increasing NBO/T, and then decreases with further NBO/T increase (Fig. 8a). Such behavior depends on the relative proportions of four-, five-, and six-coordinated Mg and Fe^{2+} cations in the melt (Kushiro and Walter, 1998; Kushiro and Mysen, 2002). In the last decades, three different second order polynomial curves have been regressed by authors for mafic terrestrial (Kushiro and Walter, 1998; Mibe et al., 2006) and Martian (Filiberto and Dasgupta, 2011) basalts. These curves are characterized by a maximum value of $K_{D(Fe-Mg)}$ at NBO/T of ~1.5-2 (Fig. 8a). The Fe^{2+}-Mg exchanges from decarbonation experiments deviate from the modeled parabolas at NBO/T >0.9, when the amount of $CaCO_3$ assimilated by melts is 20 wt.% (Fig. 8a). Despite the value of $K_{D(Fe-Mg)}$ decreases slightly with increasing CaO in the melt, the corresponding value of NBO/T increases remarkably (Fig. 8a). This behavior supports the finding that i) the effect of Ca on melt structure is much more influencing than T and ^{melt}Mg#, ii) the value of NBO/T does not account for the dominant type of network-modifying cations and the structural changes in the melt (i.e., coordination number, ionic potential, steric hindrance, and distortion of the polyhedra), and iii) the number of Ca-Fe^{2+} substitutions in olivine M2 site is bounded by the larger Ca cations relative to the smaller Fe^{2+} ones.

The geometry of M2 octahedral site and the cation size are limiting factors for the partitioning of divalent cations between olivine and melt, leading to a marked non-ideal Ca-Mg substitution (Adams and Bishop, 1985; Davidson and Mukhopadhyay, 1984; Mukhopadhyay and Lindsley, 1983; Warner and Luth, 1973; Snyder and Carmichael, 1992). Consequently, $K_{D(Ca-Mg)}$ varies in a narrow range of ~0.008-0.015, as the degree of $CaCO_3$ assimilation increases by up to 20 wt.% (Fig. 7). Moreover, the positive correlation between $K_{D(Ca-Mg)}$ and NBO/T (Fig. 8b) confirms the control of the melt structure on the cation exchange reaction. The same conclusion applies to $K_{D(Mn-Mg)}$ (Fig. 8c) and $K_{D(Ni-Mg)}$ (Fig. 8d) showing minimum values at NBO/T of ~1.5, in agreement with those found for highly depolymerized basaltic melts (Mysen, 2006). The variation of $K_{D(Ni-Mg)}$ may be addressed to either the influence of the melt structure on the solubility of Ni cations (Irvine and Kushiro, 1976; Takahashi, 1978), or the temperature dependence of the Ni-Mg exchange reaction (Matzen et al., 2013). $K_{D(Mn-Mg)}$ shows little variations with temperature (Kohn and Schofield, 1994), being mostly controlled by the effect of $CaCO_3$ assimilation (Fig. 7). This reflects the higher number of NBO coordinating Mn cations as the amount of CaO in the melt increases (Watson, 1977). Furthermore, Mn and Ca compete for the same M2 site in olivine (Fig. 1) and, consequently, less octahedral crystallographic sites are available for Mn cations during magma-carbonate interaction (Takahashi, 1978; Kohn and Schofield, 1994). It is interesting to note that the value of NBO/T does not greatly scales with ^{melt}Mg# (Fig. 8), due to an almost equal substitution between Fe^{2+} and Mg as network-modifying cations with comparable ionic potentials. Thus, the value of $K_{D(Fe-Mg)}$ is observed to weakly increase when ^{melt}Mg# decreases from 78 to 72 (Fig. 8a). In contrast, at a given NBO/T value, $K_{D(Ca-Mg)}$ (Fig. 8b), $K_{D(Mn-Mg)}$ (Fig. 8c), and $K_{D(Ni-Mg)}$ (Fig. 8d) decrease remarkably with decreasing ^{melt}Mg# or, alternatively, with increasing D_{Mg}^{2+} (Fig. 4). This demonstrates that the effect of Mg on the exchange partition coefficient is always subordinate to that of Ca, accounting for the following considerations: i) the content of MgO in the melt changes by only ~20%, whereas CaO increases markedly by ~50% and ii) the depolymerizing effect of Ca in the melt is always greater than that of Mg because Mg-NBO bonds are sterically more hindered and less energetically favored than Ca-NBO bonds (Mysen, 2008).

4.4. Applications to the primitive magmatic skarns of the Colli Albani Volcanic District

The Colli Albani Volcanic District (CAVD) is located close to the city of Rome (Italy) and is one of the main volcanic settings belonging to the ultrapotassic Roman Province (e.g., Freda et al., 2008). The eruptive products at CAVD testify to complex contamination reactions due to the emplacement of magmas within a thick carbonate sequence localized at ~2 km depth (Freda et al., 2008 and references therein). In particular, lithic clasts in pyroclastic deposits have been recognized as cumulates and skarns (either endoskarns or exoskarns) representing the rock compositional heterogeneity at the magma-carbonate interface (e.g., Gaeta et al., 2009; Di Rocco et al., 2012). The paragenesis of lithic clasts is dominated by olivine and clinopyroxene, with mineral compositions and proportions variable as a function of the degree of carbonate assimilation. The NiO vs. Fo diagram (Fig. 9a) displays the chemical changes of olivine phenocrysts found in cumulates and endoskarns at CAVD (data from Gaeta et al., 2009 and Di Rocco et al., 2012). Olivine phenocrysts from cumulates are less influenced by the effect of carbonate assimilation, showing that NiO and Fo contents decrease along a prevailing crystal fractionation path (Fig. 9a). In contrast, the composition of olivines from endoskarns is greatly controlled by the degree of carbonate assimilation, leading to the formation of NiO-poor, Fo-CaO-rich phenocrysts. Results from $^{melt}Mg\#_{78}$ decarbonation experiments confirm that Ni is less efficiently incorporated in the olivine crystal lattice, as the amount of carbonate assimilated increases from 0 to 10 to 20 wt.% (Fig. 9a). Intriguingly, natural $Fo_{94\text{-}97}$ olivines with extremely low Ni contents are not captured in full by the experimental path. These phenocrysts are found in CaO-rich endoskarns grading to the exoskarn domain close to the carbonate wall-rocks (Di Rocco et al., 2012). Therefore, $Fo_{94\text{-}97}$ olivines are the product of higher degrees of carbonate assimilation at the magma-carbonate interface (cf. Conte et al., 2009; Mollo et al., 2010, 2013a; Mollo and Vona, 2014) where calcite dissolution and magma contamination phenomena are more effective (Carter and Dasgupta, 2015, 2016). The Ni vs. CaO diagram (Fig. 9b) shows the contamination path of melt inclusions entrapped in the same olivine phenocrysts from cumulates and endoskarns (data from Gaeta et al., 2009 and Di Rocco et al., 2012). Ni is negatively correlated with CaO due to early fractionation of olivine (Gaeta et al., 2009) and dilution of the contaminated magma by carbonate assimilation (Carter and Dasgupta, 2016). The melt inclusion with the highest Ni and lowest CaO contents is used as starting composition to track the combined effects of assimilation and fractional crystallization (AFC). Olivine-melt partition coefficients of Ca (D_{Ca}^{2+} = 0.15) and Ni (D_{Ni}^{2+} = 11.22) are estimated through Eqns. 11 and 26, respectively. The CaO content of the assimilant is set to 45 wt.%, corresponding to the thermal decomposition of $CaCO_3$ (Mollo et al., 2013a). The amount of fractionated olivine is lower than 8% and the ratio of the assimilation rate to the crystallization rate changes from 0.01 to 0.2, in order to reproduce variable degrees of carbonate assimilation. Modeling results confirm that cumulates at CAVD are less affected by magma-carbonate interaction (Fig. 9b) and are produced by degrees of carbonate assimilation lower than 6% (cf. Gaeta et al., 2009; Di Rocco et al., 2012). Conversely, the geochemical signature of endoskarns accounts for stronger carbonate assimilation effects (Fig. 9b), in agreement with previous AFC calculations conducted by Di Rocco et al. (2012) using trace element and isotope data of cumulate and endoskarn rocks.

5. Summary and conclusions

Magma-carbonate interaction experiments from this study have been designed to better understand the chemical variation of olivine in primitive magmatic skarn environments, as well as to resolve the influence of temperature and bulk composition on the partitioning behavior of divalent cations between olivine crystals and decarbonated melts. Considering the wide spectrum of partitioning models reported in literature, some predictive equations can be refined to better quantify the effect of carbonate assimilation. Through this approach, the following conclusions can be drawn:

1) the crystallization of Fo-CaO-rich, NiO-poor olivines is more favored at higher temperatures when primitive basaltic melts assimilate up to 20 wt.% of carbonate material;
2) under such open-system conditions, the amount of Ca entering olivine crystal lattice is proportional to the number of Ca-O-Si bonds available in the melt structure;
3) the partitioning behavior of divalent cations between olivine and melt changes as a function of temperature, crystal composition, and melt structure. As the degree of $CaCO_3$ assimilation increases, D_{Ca}^{2+} and D_{Mg}^{2+} increase, whereas D_{Fe}^{2+}, D_{Mn}^{2+}, and D_{Ni}^{2+} decrease;

4) D_{Ca}^{2+} is prevalently controlled by CaO and MgO contents in olivine, as well as the activity of calcium in the melt (a_{CaO}^{melt});

5) D_{Mg}^{2+} is parameterized as function of a_{CaO}^{melt}, T, and MgO in the melt;

6) D_{Fe}^{2+} is a linear function of both D_{Mg}^{2+} and a_{CaO}^{melt}. Nevertheless, a log-linear relationship between D_{Fe}^{2+} and the number of non-bridging oxygens per tetrahedrally coordinated cations is also found, testifying to the primary effect of Ca on the melt structure;

7) D_{Mn}^{2+} changes responding either to the higher energy state of Mn cations in more depolymerized melts, or the progressive increase of Ca cations in the olivine M2 site;

8) D_{Ni}^{2+} is independent of olivine composition due to the fact that its value is practically controlled by the degree of melt polymerization;

9) the exchange partition coefficients between Fe^{2+}/Ca/Mn/Ni and Mg do not vary significantly as a function of T and ^{melt}Mg#. The melt structure primarily controls the values of the exchange partition coefficients;

10) $K_{D(Fe-Mg)}$ is not perfectly invariant with increasing $CaCO_3$ assimilation. Despite little fluctuations, the mean value of the Fe^{2+}-Mg exchange invariably approaches to the equilibrium condition of 0.33±0.04;

11) the comparison between natural data from cumulates and endoskarns at the Colli Albani Volcanic District (Italy) and those experimentally-derived in this study indicates that the geochemical signature of olivine phenocrysts and their melt inclusions is strictly controlled by the degree of carbonate assimilation.

Acknowledgments

We are indebted with A. Kerr as Editor in-chief of this journal, an anonymous reviewer and F. Deegan for their constructive comments that significantly improved the quality of this work. The preliminary version of this study benefited from insightful and valuable comments of Keith Putirka. Thanks go to Marcel Guillong for his support with laser ablation analyses.

References

Adams, G.E., Bishop, F.C., 1986. The olivine—clinopyroxene geobarometer: experimental results in the CaO-FeO-MgO-SiO_2 system. Contrib. to Mineral. Petrol. 94, 230-237

Adams, G.E., Bishop, F.C., 1985. An experimental investigation of thermodynamic mixing properties and unit-cell parameters of forsterite-monticellite solid solution. Am. Mineral. 70, 714-722

Akamatsu, T., Fujino, K., Kumazawa, M., Fujimura, A., Kato, M., Sawamoto, H., Yamanaka, T., 1988. Pressure and temperature dependence of cation distribution in Mg-Mn olivine. Phys. Chem. Miner. 16, 105-113

Ammannati, E., Jacob, D.E., Avanzinelli, R., Foley, S.F., Conticelli, S., 2016. Low Ni olivine in silica-undersaturated ultrapotassic igneous rocks as evidence for carbonate metasomatism in the mantle. Earth Planet. Sci. Lett. 444, 64–74. https://doi.org/10.1016/j.epsl.2016.03.039

Annersten, H., Ericsson, T., Filippidis, A., 1982. Cation Ordering in Ni-Fe Olivines. Am. Mineral. 67, 1212-1217

Barnes, C.G., Prestvik, T., Sundvoll, B., Surratt, D., 2005. Pervasive assimilation of carbonate and silicate rocks in the Hortavær igneous complex, north-central Norway. Lithos 80, 179–199. https://doi.org/10.1016/j.lithos.2003.11.002

Barr, J.A., Grove, T.L., 2013. Experimental petrology of the Apollo 15 group A green glasses: Melting primordial lunar mantle and magma ocean cumulate assimilation. Geochim. Cosmochim. Acta 106, 216-230

Beattie, P., 1993. Olivine-melt and orthopyroxene-melt equilibria. Contrib. to Mineral. Petrol. 115, 103–111

Beattie, P., Ford, C., Russell, D., 1991. Partition coefficients for olivine-melt and orthopyroxene-melt systems. Contrib. to Mineral. Petrol. 109, 212–224. https://doi.org/10.1007/BF00306480

Bédard, J.H., 2005. Partitioning coefficients between olivine and silicate melts. Lithos 83, 394–419. https://doi.org/10.1016/j.lithos.2005.03.011

Berndt, J., Koepke, J., Holtz, F., 2005. An experimental investigation of the influence of water and oxygen fugacity on differentiation of MORB at 200 MPa. J. Petrol. 46, 135–167. https://doi.org/10.1093/petrology/egh066

Bickle, M.J., Ford, C.E., Nisbet, E.G., 1977. The petrogenesis of peridotitic komatiites: evidence from high-pressure melting experiments. Earth Planet. Sci. Lett. 37, 97-106

Blundy, J.D., Wood, B.J., 1994. Prediction of crystal-melt partition coefficients from elastic moduli. Nature 372, 452–454. https://doi.org/10.1038/372452a0

Bottinga, Y., Weill, D.F., Richet, P., 1981. Thermodynamic modeling of silicate melts. In Thermodynamics of minerals and melts Springer, New York, NY, pp. 207-245

Carter, L.B., Dasgupta, R., 2016. Effect of melt composition on crustal carbonate assimilation – Implications for the transition from calcite consumption to skarnification and associated CO_2 degassing. Geochem. Geophys. Geosyst. 17, 3893–3916.

Carter, L.B., Dasgupta, R., 2015. Hydrous basalt-limestone interaction at crustal conditions: Implications for generation of ultracalcic melts and outflux of CO_2 at volcanic arcs. Earth Planet. Sci. Lett. 427, 202–214. https://doi.org/10.1016/j.epsl.2015.06.053

Chadwick, J.P., Troll, V.R., Ginibre, C., Morgan, D., Gertisser, R., Waight, T.E., Davidson, J.P., 2007. Carbonate assimilation at Merapi Volcano, Java, Indonesia: Insights from crystal isotope stratigraphy. J. Petrol. 48, 1793–1812. https://doi.org/10.1093/petrology/egm038

Clague, D.A., Weber, W.S., Dixon, J.E., 1991. Picritic glasses from Hawaii. Nature 353, 553

Colson, R.O., McKay, G.A., Taylor, L.A., 1989. Charge balancing of trivalent trace elements in olivine and low-Ca pyroxene: A test using experimental partitioning data. Geochim. Cosmochim. Acta 53, 643–648. https://doi.org/10.1016/0016-7037(89)90007-0

Connolly, J.A.D., Cesare, B., 1993. C- O- H- S fluid composition and oxygen fugacity in graphitic metapelites. J. Metamorph. Geol. 11, 379-388

Conte, A.M., Dolfi, D., Gaeta, M., Misiti, V., Mollo, S., Perinelli, C., 2009. Experimental constraints on evolution of leucite-basanite magma at 1 and 10^{-4} GPa: implications for parental compositions of Roman high-potassium magmas. Eur. J. Mineral. 21, 763–782. https://doi.org/10.1127/0935-1221/2009/0021-1934

Coogan, L.A., Hain, A., Stahl, S., Chakraborty, S., 2005. Experimental determination of the diffusion coefficient for calcium in olivine between 900°C and 1500°C. Geochim. Cosmochim. Acta 69, 3683–3694. https://doi.org/10.1016/j.gca.2005.03.002

Coulson, I.M., Westphal, M., Anderson, R.G., Kyser, T.K., 2007. Concomitant skarn and syenitic magma evolution at the margins of the Zippa Mountain pluton. Mineral. Petrol. 90, 199-221

Dallai, L., Cioni, R., Boschi, C., D'Oriano, C., 2011. Carbonate-derived CO2purging magma at depth: Influence on the eruptive activity of Somma-Vesuvius, Italy. Earth Planet. Sci. Lett. 310, 84–95. https://doi.org/10.1016/j.epsl.2011.07.013

Danyushevsky, L.V., Plechov, P., 2011. Petrolog3: Integrated software for modeling crystallization processes. Geochem. Geophys. Geosyst., 12, Q07021.

Davidson, P.M., Mukhopadhyay, D.K., 1984. Ca-Fe-Mg olivines: phase relations and a solution model. Contrib. Mineral. Petrol. 86, 256-263

Deegan, F.M., Troll, V.R., Freda, C., Misiti, V., Chadwick, J.P., McLeod, C.L., Davidson, J.P., 2010. Magma–carbonate interaction processes and associated CO2 release at Merapi Volcano, Indonesia: insights from experimental petrology. Journal of Petrology 51, 1027–1051

DePaolo, D.J., 1981. Trace element and isotopic effects of combined wall rock assimilation and fractional crystallization. Earth Planet. Sci. Lett. 53, 189-202

Del Bello, E., Mollo, S., Scarlato, P., von Quadt, A., Forni, F., Bachmann, O., 2014. New petrological constraints on the last eruptive phase of the Sabatini Volcanic District (central Italy): Clues from mineralogy, geochemistry, and Sr-Nd isotopes. Lithos 205, 28–38. https://doi.org/10.1016/j.lithos.2014.06.015

Di Battistini, G., Montanini, A., Vernia, L., Venturelli, G., Tonarini, S., 2001. Petrology of melilite-bearing rocks from the Montefiascone Volcanic Complex (Roman Magmatic Province): New insights into the ultrapotassic volcanism of Central Italy. Lithos 59, 1–24. https://doi.org/10.1016/S0024-4937(01)00054-8

Di Rocco, T., Freda, C., Gaeta, M., Mollo, S., Dallai, L., 2012. Magma chambers emplaced in carbonate substrate: Petrogenesis of skarn and cumulate rocks and implications for CO_2 degassing in volcanic areas. J. Petrol. 53, 2307–2332. https://doi.org/10.1093/petrology/egs051

Doroshkevich, A.G., Ripp, G.S., Izbrodin, I.A., Savatenkov, V.M., 2012. Alkaline magmatism of the Vitim province, West Transbaikalia, Russia: Age, mineralogical, geochemical and isotope (O, C, D, Sr and Nd) data. Lithos 152, 157-172

Dunitz, J.D., Orgel, L.E., 1957. Electronic properties of transition-metal oxides—I: Distortions from cubic symmetry. J. Phys. Chem. Solids 3, 20-29

Dunn, T., 1987. Partitioning of Hf, Lu, Ti, and Mn between olivine, clinopyroxene and basaltic liquid. Contrib. Mineral. Petrol. 96, 476– 484

Dunworth, E.A., Wilson, M., 1998. Olivine melilitites of the SW German Tertiary volcanic province: Mineralogy and petrogenesis. J. Petrol. 39, 1805–1836. https://doi.org/10.1093/petroj/39.10.1805

Ferguson, A.K., 1978. Ca-enrichment in olivines from volcanic rocks. Lithos 11, 189–194. https://doi.org/10.1016/0024-4937(78)90019-1

Filiberto, J., Dasgupta, R., 2011. Fe^{2+}-Mg partitioning between olivine and basaltic melts: Applications to genesis of olivine-phyric shergottites and conditions of melting in the Martian interior. Earth Planet. Sci. Lett. 304, 527–537. https://doi.org/10.1016/j.epsl.2011.02.029

Foland, K.A., Landoll, J.D., Henderson, C.M.B., Chen, J., 1993. Formation of cogenetic quartz and nepheline syenites. Geochim. Cosmochim. Acta 57, 697-704

Ford, C.E., Russel, D.G., Craven, J.A., Fisk, M.R., 1983. Olivine-Liquid Equilibria: Temperature, Pressure and Composition Dependence of the Crystal/Liquid Cation Partition Coefficients for Mg, Fe^{2+}, Ca and Mn. J. Petrol. 24, 256–266. https://doi.org/10.1093/petrology/24.3.256

Francis, C.A., Ribbe, P.H., 1980. The forsterite-tephroite series: I. Crystal structure refinements. Am. Mineral. 65, 1263-1269

Freda, C., Gaeta, M., Giaccio, B., Marra, F., Palladino, D.M., Scarlato, P., Sottili, G., 2011. CO_2-driven large mafic explosive eruptions: the Pozzolane Rosse case study from the Colli Albani Volcanic District (Italy). Bulletin of Volcanology 73, 241–256.

Freda, C., Gaeta, M., Misiti, V., Mollo, S., Dolfi, D., Scarlato, P., 2008. Magma-carbonate interaction: An experimental study on ultrapotassic rocks from Alban Hills (Central Italy). Lithos 101, 397–415. https://doi.org/10.1016/j.lithos.2007.08.008

Fulignati, P., Marianelli, P., Santacroce, R., Sbrana, A., 2004. Probing the Vesuvius magma chamber-host rock interface through xenoliths. Geol. Mag. 141, 417–428. https://doi.org/10.1017/S0016756804009392

Fulignati, P., Marianelli, P., Santacroce, R., Sbrana, A., 2000. The skarn shell of the 1944 Vesuvius magma chamber. Genesis and PTX conditions from melt and fluid inclusion data. Eur. J. Mineral. 12, 1025–1039. https://doi.org/10.1127/0935-1221/2000/0012-1025

Gaeta, M., Di Rocco, T., Freda, C., 2009. Carbonate assimilation in open magmatic systems: The role of melt-bearing skarns and cumulate-forming processes. J. Petrol. 50, 361–385. https://doi.org/10.1093/petrology/egp002

Gaetani, G.A., 2004. The influence of melt structure on trace element partitioning near the peridotite solidus. Contrib. to Mineral. Petrol. 147, 511–527. https://doi.org/10.1007/s00410-004-0575-1

Galoisy, L., Calas, G., Brown, G.E., 1995. Intracrystalline distribution of Ni in San Carlos olivine: an EXAFS study. Am. Mineral. 80, 1089–1092

Gee, L.L., Sack, R.O., 1988. Experimental petrology of melilite nephelinites. J. Petrol. 29, 1233-1255

Gozzi, F., Gaeta, M., Freda, C., Mollo, S., Di Rocco, T., Marra, F., Dallai, L., Pack, A., 2014. Primary magmatic calcite reveals origin from crustal carbonate. Lithos 190–191, 191–203. https://doi.org/10.1016/j.lithos.2013.12.008

Hart, S.R., Davis, K.E., 1978. Nickel partitioning between olivine and silicate melt. Earth Planet. Sci. Lett. 40, 203-219

Hayes, B., Lissenberg, C.J., Bédard, J.H., Beard, C., 2015. The geochemical effects of olivine slurry replenishment and dolostone assimilation in the plumbing system of the Franklin Large Igneous Province, Victoria Island, Arctic Canada. Contrib. to Mineral. Petrol. 169. https://doi.org/10.1007/s00410-015-1117-8

Heinemann, R., Staack, V., FIscher, A., Kroll, H., Vad, T., Kirfel, A., 1999. Temperature dependence of Fe, Mg partitioning in Acapulco olivine. Am. Mineral. 84, 1400–1405

Henderson, P., Dale, I.M., 1970. The partitioning of selected transition element ions between olivine and groundmass of oceanic basalts. Chem. Geol. 3, 267–274

Henderson, C.M.B., Knight, K.S., Redfern, S.A.T., Wood, B.J., 1996. High-temperature study of octahedral cation exchange in olivine by neutron powder diffraction. Science 271, 1713-1715

Herzberg, C., O'hara, M.J., 1998. Phase equilibrium constraints on the origin of basalts, picrites, and komatiites. Earth Sci. Rev. 44, 39-79

Huang, F., Lundstrom, C.C., McDonough, W.F., 2006. Effect of melt structure on trace-element partitioning between clinopyroxene and silicic, alkaline, aluminous melts. Am. Mineral. 91, 1385–1400. https://doi.org/10.2138/am.2006.1909

Iacono Marziano, G., Gaillard, F., Scaillet, B., Pichavant, M., Chiodini, G., 2009. Role of non-mantle CO_2 in the dynamics of volcano degassing: The Mount Vesuvius example. Geology, 37, 319-322

Iacono Marziano, G., Gaillard, F., Pichavant, M., 2008. Limestone assimilation by basaltic magmas: an experimental re-assessment and application to Italian volcanoes. Contrib. to Mineral. Petrol. 155, 719-738

Irvine, T.N., 1982. Terminology for layered intrusions. J. Petrol. 23, 127–162. https://doi.org/10.1093/petrology/23.2.127-a

Irvine, T.N., Kushiro, I., 1976. Partitioning of Ni and Mg between olivine and silicate liquids. Carnegie Inst. Wash. Yearb. 75, 668-675

Jaeger, W.L., Drake, M.J., 2000. Metal–silicate partitioning of Co, Ga, and W: dependence on silicate melt composition. Geochim. Cosmochim. Acta 64, 3887-3895

Jackson, W.E., Farges, F., Yeager, M., Mabrouk, P.A., Rossano, S., Waychunas, G.A., Solomon, E.I., Brown, G.E., 2005. Multispectroscopic study of Fe(II) in silicate glasses: implications for the coordination environment of Fe(II) in silicate melts. Geochim. Cosmochim. Acta 69, 4315–4332

Jana, D., Walker, D., 1997. The influence of sulfur on partitioning of siderophile elements. Geochim. Cosmochim. Acta 61, 5255-5277

Jolis, E.M., Troll, V.R, Harris, C., Freda, C., Gaeta, M., Orsi G, Siebe, C., 2015. Skarn xenolith record crustal CO2 liberation during Pompeii and Pollena eruptions, Vesuvius volcanic system, central Italy. Chemical Geology 415, 17–36

Jolis, E.M., Freda, C., Troll, V.R., Deegan, F.M., Blythe, L.S., McLeod, C.L., Davidson, J.P., 2013. Experimental simulation of magma-carbonate interaction beneath Mt. Vesuvius, Italy. Contrib. to Mineral. Petrol. 166, 1335–1353. https://doi.org/10.1007/s00410-013-0931-0

Jones, J.H., 2016. Thoughts and Reminiscences on Experimental Trace Element Partitioning. Geochemical Perspect. 5, 147–251. https://doi.org/10.7185/geochempersp.5.2

Jones, J.H., 1995. Experimental trace element partitioning. In: Ahrens, T.J. (Ed.) Rock Physics and Phase Relations, A Handbook of Physical Constants. AGU Reference Shelf 3, American Geophysical Union, Washington, D.C., USA, 73-104

Jones, J.H., 1988. Partitioning of Mg and Fe between olivine and liquids of lunar compositions: the roles of composition, pressure, and Ti speciation (Abstract). In: Lunar Planetary Science XIX. Lunar and Planetary Institute, Houston, USA, 561-562

Jones, J.H., 1984. Temperature and pressure-independent correlations of olivine liquid partition coefficients and their application to trace element partitioning. Contrib. to Mineral. Petrol. 88, 126–132

Jurewicz, A.J.G., Watson, E.B., 1988. Cations in olivine, Part 2: Diffusion in olivine xenocrysts, with applications to petrology and mineral physics. Contrib. to Mineral. Petrol. 99, 186–201. https://doi.org/10.1007/BF00371460

Keppler, H., 1992. Crystal field spectra and geochemistry of transition metal ions in silicate melts and glasses. Am. Mineral. 77, 62–75

Keppler, H., Bagdassarov, N.S., 1999. The speciation of Ni and Co in silicate melts from optical absorption spectra to 1500°C. Chem. Geol. 158, 105–115

Kohn, S.C., Schofield, P.F., 1994. The importance of melt composition in controlling trace-element behaviour: an experimental study of Mn and Zn partitioning between forsterite and silicate melts. Chem. Geol. 117, 73–87. https://doi.org/10.1016/0009-2541(94)90122-8

Korenaga, J., Kelemen, P.B., 2000. Major element heterogeneity in the mantle source of the North Atlantic igneous province. Earth Planet. Sci. Lett. 184, 251-268

Kress, V.C., Carmichael, I.S., 1991. The compressibility of silicate liquids containing Fe_2O_3 and the effect of composition, temperature, oxygen fugacity and pressure on their redox states. Contrib. to Mineral. Petrol. 108, 82-92

Kushiro, I., Mysen, B.O., 2002. A possible effect of melt structure on the Mg-Fe partitioning between olivine and melts. Geochim. Cosmochim. Acta 66, 2267–2272

Kushiro, I., Walter, M.J., 1998. Mg-Fe partitioning between olivine and mafic-ultramafic melts. Geophys. Res. Lett. 25, 2337–2340. https://doi.org/10.1029/98GL01844

Langmuir, C.H., Hanson, G.N., 1981. Calculating Mineral—Melt Equilibria with Stoichiometry, Mass Balance, and Single-Component Distribution Coefficients. In Thermodynamics of minerals and melts Springer, New York, NY, pp. 247-271

Le Bas, M., Maitre, R.L., Streckeisen, A., Zanettin, B., IUGS Subcommission on the Systematics of Igneous Rocks, 1986. A chemical classification of volcanic rocks based on the total alkali-silica diagram. J. Petrol. 27, 745-750

Lee, S.K., Stebbins, J.F., 2003. The distribution of sodium ions in aluminosilicate glasses: a high-field Na-23 MAS and 3Q MAS NMR study. Geochim. Cosmochim. Acta 67, 1699-1709

Leeman, W.P., 1978. Distribution of Mg^{2+} between olivine and silicate melt, and its implications regarding melt structure. Geochim. Cosmochim. Acta 42, 789–800

Leeman, W.P., Scheidegger, K.F., 1977. Olivine/liquid distribution coefficients and a test for crystal-liquid equilibrium. Earth Planet. Sci. Lett. 35, 247-257

Lentz, D.R., 1999. Petrology, geochemistry, and oxygen isotope interpretation of felsic volcanic and related rocks hosting the Brunswick 6 and 12 massive sulfide deposits (Brunswick Belt), Bathurst mining camp, New Brunswick, Canada. Econ. Geol. 94, 57-86

Li, C., Ripley, E.M., 2010. The relative effects of composition and temperature on olivine-liquid Ni partitioning: Statistical deconvolution and implications for petrologic modeling. Chem. Geol. 275, 99–104. https://doi.org/10.1016/j.chemgeo.2010.05.001

Libourel, G., 1999. Systematics of calcium partitioning between olivine and silicate melt: Implications for melt structure and calcium content of magmatic olivines. Contrib. to Mineral. Petrol. 136, 63–80. https://doi.org/10.1007/s004100050524

Libourel, G., Boivin, P., Biggar, G.M., 1989. The univariant curve liquid=forsterite+anorthite+diopside in the system CMAS at 1 bar: solid solutions and melt structure. Contrib. to Mineral. Petrol. 102, 406-421

Longhi, J., Pan, V., 1988. A reconnaisance study of phase boundaries in low-alkali basaltic liquids. J. Petrol. 29, 115-147

Longhi, J., Walker, D., Hays, J.F., 1978. The distribution of Fe and Mg between olivine and lunar basaltic liquids. Geochim. Cosmochim. Acta 42, 1545-1558

Lumpkin, G.R., Ribbe, P.H., Lumpkin, N.E., 1983. Composition, order-disorder and lattice parameters of olivines; determinative methods for Mg-Mn and Mg-Ca silicate olivines. Am. Mineral. 68, 1174-1182

Lynn, K.J., Shea, T., Garcia, M.O., 2017. Nickel variability in Hawaiian olivine: Evaluating the relative contributions from mantle and crustal processes. Am. Mineral. 102, 507-518

Maekawa, H., Maekawa, T., Kawamura, K., Yokokawa, T., 1991. The structural groups of alkali silicate glasses determined from 29Si MAS-NMR. J. Non-Cryst. Solids 127, 53-64

Mason, E., Edmonds, M., Turchyn, A.V., 2017. Remobilization of crustal carbon dominates volcanic arc emissions. Science 357, 290-294. https://doi.org/10.1126/science.aan5049

Matzen. A.K., Baker, M.B., Beckett, J.R., Wood, B.J., Stolper, E.M., 2017. The effect of liquid composition on the partitioning of Ni between olivine and silicate melt. Contrib. to Mineral. Petrol. 172, 1–18. https://doi.org/10.1007/s00410-016-1319-8

Matzen, A.K., Baker, M.B., Beckett, J.R., Stolper, E.M., 2013. The temperature and pressure dependence of nickel partitioning between olivine and silicate melt. J. Petrol. 54, 2521–2545. https://doi.org/10.1093/petrology/egt055

Matzen, A.K., Baker, M.B., Beckett, J.R., Stolper, E.M., 2011. Fe-Mg partitioning between olivine and high-magnesian melts and the nature of Hawaiian parental liquids. J. Petrol. 52, 1243–1263. https://doi.org/10.1093/petrology/egq089

Mibe, K., Orihashi, Y., Nakai, S., Fujii, T., 2006. Element partitioning between transition-zone minerals and ultramafic melt under hydrous conditions. Geophys. Res. Lett. 33, 1–6. https://doi.org/10.1029/2006GL026999

Mollo, S., Hammer, J.E., 2017. Dynamic crystallization in magmas. In Mineral reaction kinetics: microstructures, textures, chemical and isotopic signatures. Edited by W. Heinrich and R. Abart. EMU Notes in Mineralogy, Vol. 16 (2016), Chapter 7, 1–46. Published by the European

Mineralogical Union and the Mineralogical Society of Great Britain & Ireland. Doi: 10.1180/EMU-notes.16.12

Mollo, S., Forni F., Bachmann, O., Blundy, J.D., De Astis, G., Scarlato, P., 2016. Trace element partitioning between clinopyroxene and trachy-phonolitic melts: A case study from the Campanian ignimbrite (Campi Flegrei, Italy), Lithos 252–253, 160–172, doi:10.1016/j.lithos.2016.02.024

Mollo, S., Giacomoni, P.P., Coltorti, M., Ferlito, C., Iezzi, G., Scarlato, P., 2015. Reconstruction of magmatic variables governing recent Etnean eruptions: constraints from mineral chemistry and P-T-fO2-H2O modelling, Lithos, 212-215, 311-320, 10.1016/j.lithos.2014.11.020

Mollo, S., Vona, A., 2014. The geochemical evolution of clinopyroxene in the Roman Province: A window on decarbonation from wall-rocks to magma, Lithos 192-195, 1-7, 10.1016/j.lithos.2014.01.009

Mollo, S., Heap, M.J., Dingwell, D.B., Hess, K.U., Iezzi, G., Masotta, M., Scarlato, P., Vinciguerra, S., 2013a. Decarbonation and thermal microcracking under magmatic P-T-fCO_2 conditions: the role of skarn substrata in promoting volcanic instability, Geophysical Journal International 195, 369-380, doi: 10.1093/gji/ggt265

Mollo, S., Blundy, J.D., Scarlato, P., Iezzi, G., Langone, A., 2013b, The partitioning of trace elements between clinopyroxene and trachybasaltic melt during rapid cooling and crystal growth, Contrib. to Mineral. Petrol. 166, 1633-1654, doi: 10.1007/s00410-013-0946-6

Mollo, S., Putirka, K.D., Iezzi, G., Scarlato, P., 2013c. The control of cooling rate on titanomagnetite composition: Implications for a geospeedometry model applicable to alkaline rocks from Mt. Etna volcano, Contrib. to Mineral. Petrol. 165, 457–475, doi: 10.1007/s00410-012-0817-6

Mollo, S., Scarlato, P., Freda, C., Gaeta, M., 2011. Basalt-crust interaction processes: insights from experimental petrology, pp. 33-61, in West, J.P., eds., Basalt: Types, Petrology and Uses: New York, Nova Science Publishers, pp. 189. ISBN: 9781612096353

Mollo, S., Gaeta, M., Freda, C., Di Rocco, T., Misiti, V., Scarlato, P., 2010. Carbonate assimilation in magmas: A reappraisal based on experimental petrology. Lithos 114, 503-514, doi: 10.1016/j.lithos.2009.10.013

Mukhopadhyay, D.K., Lindsley, D.H., 1983. Phase relations in the join kirschsteinite - fayalite. Am. Mineral. 68, 1089–1094.

Mysen, B.O., 2008. Olivine/melt transition metal partitioning, melt composition, and melt structure-Melt polymerization and Qn-speciation in alkaline earth silicate systems. Geochim. Cosmochim. Acta 72, 4796–4812. https://doi.org/10.1016/j.gca.2008.07.010

Mysen, B.O., 2007. The solution behavior of H_2O in peralkaline aluminosilicate melts at high pressure with implications for properties of hydrous melts. Geochim. Cosmochim. Acta 71, 1820-1834

Mysen, B.O., 2006. Redox equilibria of iron and silicate melt structure: Implications for olivine/melt element partitioning. Geochim. Cosmochim. Acta 70, 3121–3138. https://doi.org/10.1016/j.gca.2006.03.014

Mysen, B.O., 2004. Element partitioning between minerals and melt, melt composition, and melt structure. Chem. Geol. 213, 1-16

Mysen, B.O., Richet, P., 2005. Silicate glasses and melts: properties and structure. Elsevier, New York, pp. 548

Mysen, B.O., Dubinsky, E.V., 2004. Melt structural control on olivine/melt element partitioning of Ca and Mn1. Geochim. Cosmochim. Acta 68, 1617-1633.

Mysen, B.O., Virgo, D., 1980. Trace element partitioning and melt structure: An experimental study at 1 atm pressure. Geochim. Cosmochim. Acta 44, 1917–1930. https://doi.org/10.1016/0016-7037(80)90191-X

Mysen, B.O., Carmichael, I.S.E., Virgo, D., 1985. A comparison of iron redox ratios in silicate glasses determined by wet-chemical and 57 Fe Mössbauer resonant absorption methods. Contrib. to Mineral. Petrol. 90, 101-106

Mysen, B.O., Virgo, D., Seifert, F.A., 1982. The structure of silicate melts: implications for chemical and physical properties of natural magma. Reviews of Geophysics 20, 353-383

Nielsen R.L., Davidson P.M., Grove T.L., 1988. Pyroxene-melt equilibria: an updated model. Contrib. to Mineral. Petrol. 100, 361-373

Papike, J.J., Karner, J.M., Shearer, C.K., 2005. Comparative planetary mineralogy: Valence state partitioning of Cr, Fe, Ti, and V among crystallographic sites in olivine, pyroxene, and spinel from planetary basalts. Am. Mineral. 90, 277–290. https://doi.org/10.2138/am.2005.1779

Patiño Douce, A.E., 1999. What do experiments tell us about the relative contributions of crust and mantle to the origin of granitic magmas? Geological Society, London, Special Publications 168, 55-75

Pu, X., Lange, R.A., Moore, G., 2017. A comparison of olivine-melt thermometers based on DMg and DNi: The effects of melt composition, temperature, and pressure with applications to MORBs and hydrous arc basalts. Am. Mineral. 102, 750–765. https://doi.org/10.2138/am-2017-5879

Putirka, K.D., 2016. Rates and styles of planetary cooling on Earth, Moon, Mars, and Vesta, using new models for oxygen fugacity, ferric-ferrous ratios, olivine-liquid Fe-Mg exchange, and mantle potential temperature. Am. Mineral. 101, 819–840. https://doi.org/doi:10.2138/am-2016-5402

Putirka, K.D., 2005. Mantle potential temperatures at Hawaii, Iceland, and the mid-ocean ridge system, as inferred from olivine phenocrysts: Evidence for thermally driven mantle plumes. Geochemistry, Geophys. Geosystems 6, 1–14. https://doi.org/10.1029/2005GC000915

Putirka, K.D., Ryerson, F.J., Perfit, M., Ridley, W.I., 2011. Mineralogy and composition of the oceanic mantle. J. Petrol. 52, 279–313. https://doi.org/10.1093/petrology/egq080

Putirka, K.D., Perfit, M., Ryerson, F.J., Jackson, M.G., 2007. Ambient and excess mantle temperatures, olivine thermometry, and active vs. passive upwelling. Chem. Geol. 241, 177–206. https://doi.org/10.1016/j.chemgeo.2007.01.014

Redfern, S.A.T., Henderson, C.M.B., Wood, B.J., Harrison, R.J., Knight, K.S., 1996. Determination of olivine cooling rates from metal-cation ordering. Nature 381, 407

Redi, D., Cannatelli, C., Esposito, R., Lima, A., Petrosino, P., De Vivo, B., 2017. Somma-Vesuvius' activity: a mineral chemistry database. Mineral. Petrol. 111, 43–67. https://doi.org/10.1007/s00710-016-0462-2

Rein, R.H., Chipman, J., 1965. Activities in liquid solution SiO_2-CaO-MgO-Al_2O_3 at 1600°C. Transactions of the Metallurgical Society of AIME 233, 415

Roeder, P.L., 1974. Activity of iron and olivine solubility in basaltic liquids. Earth Planet. Sci. Lett. 23, 397-410

Roeder, P.L., Emslie, R.F., 1970. Olivine-Liquid Equilibrium. Contrib. to Mineral. Petrol. 29, 275–289

Sack, R.O., Walker, D., Carmichael, I.S., 1987. Experimental petrology of alkalic lavas: constraints on cotectics of multiple saturation in natural basic liquids. Contrib. to Mineral. Petrol. 96, 1-23

Schmidt, M.W., 2006. Element Partitioning: The Role of Melt Structure and Composition. Science 312, 1646–1650. https://doi.org/10.1126/science.1126690

Shi, P., 1993. Low pressure phase relationships in the system Na_2O-CaO-FeO-MgO-Al_2O_3-SiO_2 at 1100°C, with implications for the differentiation of basaltic magmas. J Petrol 34, 743-762

Shi, P., Libourel, G., 1991. The effects of FeO on the system CMAS at low pressure and implications for basalt crystallization processes. Contrib. to Mineral. Petrol. 108, 129-145

Snyder, D.A., Carmichael, I.S.E., 1992. Olivine-liquid equilibria and the chemical activities of FeO, NiO, Fe_2O_3, and MgO in natural basic melts. Geochim. Cosmochim. Acta 56, 303–318. https://doi.org/10.1016/0016-7037(92)90135-6

Snyder, D., Carmichael, I.S.E., Wiebe, R.A., 1993. Experimental study of liquid evolution in an Fe-rich, layered mafic intrusion: constraints of Fe-Ti oxide precipitation on the T-fO_2 and T-P paths of tholeiitic magmas. Contrib. to Mineral. Petrol. 113, 73-86

Sobolev, A.V., Hofmann, A.W., Kuzmin, D.V., Yaxley, G.M., Arndt, N.T., Chung, S.L., Gurenko, A.A., 2007. The amount of recycled crust in sources of mantle-derived melts. Science 316, 412-417

Sobolev, A.V., Hofmann, A.W., Sobolev, S.V., Nikogosian, I.K., 2005. An olivine-free mantle source of Hawaiian shield basalts. Nature 434, 590

Spandler, C., Martin, L.H.J., Pettke, T., 2012. Carbonate assimilation during magma evolution at Nisyros (Greece), South Aegean Arc: Evidence from clinopyroxenite xenoliths. Lithos 146-147, 18-33

Spera, F.J., Bohrson, W.A., 2004. Open-system magma chamber evolution: An energy-constrained geochemical model incorporating the effects of concurrent eruption, recharge, variable assimilation and fractional crystallization (EC-E′ RAχFC). J. Petrol. 45, 2459-2480

Spera, F.J., Bohrson, W.A., 2001. Energy-constrained open-system magmatic processes I: General model and energy-constrained assimilation and fractional crystallization (EC-AFC) formulation. J. Petrol. 42, 999-1018

Stormer, J.C., Nicholls, J., 1978. XLFRAC: a program for the interactive testing of magmatic differentiation models. Comput. Geosci. 4, 143–159. https://doi.org/10.1016/0098-3004(78)90083-3

Takahashi, E., 1978. Partitioning of Ni^{2+}, Co^{2+}, Fe^{2+}, Mn^{2+} and Mg^{2+} between olivine and silicate melts: compositional dependence of partition coefficient. Geochim. Cosmochim. Acta 42, 1829-1844

Thibault, Y., Walter, M.J., 1995. The influence of pressure and temperature on the metal-silicate partition coefficients of nickel and cobalt in a model C1 chondrite and implications for metal segregation in a deep magma ocean. Geochim. Cosmochim. Acta 59, 991-1002

Toplis, M.J., 2005. The thermodynamics of iron and magnesium partitioning between olivine and liquid: Criteria for assessing and predicting equilibrium in natural and experimental systems. Contrib. to Mineral. Petrol. 149, 22–39. https://doi.org/10.1007/s00410-004-0629-4

Toplis, M.J., Carroll, M.R., 1995. An experimental study of the influence of oxygen fugacity on Fe-Ti oxide stability, phase relations, and mineral—melt equilibria in ferro-basaltic systems. J. Petrol. 36, 1137-1170

Troll, V.R., Deegan, F.M., Jolis, E.M., Harris, C., Chadwick, J.P., Gertisser, R., Preece, K., 2013. Magmatic differentiation processes at Merapi Volcano: inclusion petrology and oxygen isotopes. J. Volcanol. Geotherm. Res. 261, 38-49

Troll, V.R., Hilton, D.R., Jolis, E.M., Chadwick, J.P., Blythe, L.S., Deegan, F.M., Zimmer, M., 2012. Crustal CO_2 liberation during the 2006 eruption and earthquake events at Merapi volcano, Indonesia. Geophys. Res. Lett. 39

Vetere, F., Sato, H., Ishibashi, H., De Rosa, R., Donato, P., Ishebashi, H., De Rosa, R., Donato, P., 2013. Viscosity changes during crystallization of a shoshonitic magma: new insights on lava flow emplacement. J. Mineral. Petrol. Sci. 108, 144–160. https://doi.org/10.2465/jmps.120724

Wagner, T.P., Grove, T.L., 1997. Experimental constraints on the origin of lunar high-Ti ultramafic glasses. Geochim. Cosmochim. Acta 61, 1315-1327

Wang, Z., Gaetani, G.A., 2008. Partitioning of Ni between olivine and siliceous eclogite partial melt: Experimental constraints on the mantle source of Hawaiian basalts. Contrib. to Mineral. Petrol. 156, 661–678. https://doi.org/10.1007/s00410-008-0308-y

Watson, E.B., 1977. Partitioning of manganese between forsterite and silicate liquid. Geochim. Cosmochim. Acta 41, 1363–1374. https://doi.org/10.1016/0016-7037(77)90079-5

Wenzel, T., Baumgartner, L.P., Konnikov, E.G., Bru, G.E., Kislov, E. V, 2002. Partial Melting and Assimilation of Dolomitic Xenoliths by Mafic Magma: the Ioko-Dovyren Intrusion (North Baikal Region, Russia). J. Petrol. 43, 2049–2074. https://doi.org/10.1093/petrology/43.11.2049

Wenzel, T., Baumgartner, L.P., Brügmann, G.E., Konnikov, E.G., Kislov, E. V., Orsoev, D.A., 2001. Contamination of mafic magma by partial melting of dolomitic xenoliths. Terra Nov. 13, 197–202. https://doi.org/10.1046/j.1365-3121.2001.00340.x

Warner, R.D., Luth, W.C., 1973. Data for the Join Monticellite ($CaMgSiO_4$) – Forsterite (Mg_2SiO_4): Experimental Results and Numerical Analysis. Am. Mineral. 58, 998–1008

Wood, B.J., 1974. The solubility of alumina in orthopyroxene coexisting with garnet. Contrib. to Mineral. Petrol. 46, 1-15

Wood, B.J., Blundy, J.D., 1997. A predictive model for rare earth element partitioning between clinopyroxene and anhydrous silicate melt. Contrib. to Mineral. Petrol. 129, 166–181. https://doi.org/10.1007/s004100050330

Figure captions

Fig. 1. Variation of major oxides in olivine from magma-carbonate interaction experiments. Error bars are not observable if they are smaller than the symbols.

Fig. 2. Variation of olivine components from magma-carbonate interaction experiments. The solution model refers to four end-members: forsterite, fayalite, calcio-olivine (i.e., larnite), and tephroite. Error bars are not observable if they are smaller than the symbols.

Fig. 3. Relationship between olivine and melt compositional variations as a function of temperature, $CaCO_3$, and ^{melt}Mg#. a_{MgO}^{melt}, a_{CaO}^{melt}, and $a_{SiO_2}^{melt}$ come from the magnesium, calcium, and silicon pseudo-activity models of Leeman (1978), Libourel (1999), and Bottinga at al. (1981), respectively. Error bars are not observable if they are smaller than the symbols.

Fig. 4. Olivine-melt partition coefficients of Ni, Mg, Fe^{2+}, Mn, and Ca from magma-carbonate interaction experiments. Error bars are not observable if they are smaller than the symbols.

Fig. 5. $\ln D_i^{2+}$ vs. 1/*T* diagram showing the linear correlation between divalent partition coefficient and temperature (a). $\ln D_i^{2+}$ vs. a_{CaO}^{melt} diagram showing the linear correlation between divalent partition coefficient and calcium activity in the melt (b). Straight lines refers to regression fits (see the text for further details). Error bars are not observable if they are smaller than the symbols.

Fig. 6. D_{Mn}^{2+} vs. NBO/T diagram showing the partitioning behavior of Mn from magma-carbonate interaction experiments in comparison with previous data from literature reported in Bédard (2005). Error bars are not observable if they are smaller than the symbols.

Fig. 7. Olivine-melt exchange partition coefficients between Fe^{2+}/Ca/Mn/Ni and Mg from magma-carbonate interaction experiments. Error bars are not observable if they are smaller than the symbols.

Fig. 8. $K_{D(Fe-Mg)}$ (a), $K_{D(Ca-Mg)}$ (b), $K_{D(Mn-Mg)}$ (c), and $K_{D(Ni-Mg)}$ (d) from magma-carbonate interaction experiments are plotted against the value of NBO/T. Error bars are not observable if they are smaller than the symbols.

Fig. 9. Natural products from the Colli Albani Volcanic District (CAVD) in Italy are compared with those from this study. The NiO vs. Fo diagram displays the chemical changes of olivine phenocrysts found in cumulates and endoskarns at CAVD (a). Results from ^{melt}Mg#$_{78}$ decarbonation experiments confirm that Ni is negatively correlated with Fo, as the amount of carbonate assimilated increases from 0 to 10 to 20 wt.%. The Ni vs. CaO diagram shows the contamination path of melt inclusions entrapped in the same olivine phenocrysts (b). The melt inclusion with the highest Ni and lowest CaO contents is used as starting composition to track the combined effects of assimilation and fractional crystallization (AFC). Olivine-melt partition coefficients of Ca (D_{Ca}^{2+} =

0.15) and Ni (D_{Ni}^{2+} = 11.22) are estimated through Eqns. 11 and 26, respectively. The CaO content of the assimilant is set to 45 wt.%. The amount of fractionated olivine is lower than 8% and the ratio of the assimilation rate to the crystallization rate changes from 0.01 to 0.2. Natural data from Gaeta et al., 2009 and Di Rocco et al., 2012).

Fig. 1S. D_{Ca}^{2+} values measured from magma-carbonate interaction experiments vs. those predicted by the models of Snyder and Carmichael (1992) (a), Libourel (1999) (b), and this study (c).

Fig. 2S. D_{Mg}^{2+} values measured from magma-carbonate interaction experiments vs. those predicted by the models of Beattie (1993) (a), Putirka et al. (2007) (b), Pu et al. (2017) (c), and this study (d).

Fig. 3S. D_{Fe}^{2+} values measured from magma-carbonate interaction experiments vs. those predicted by the models of Jones (2016) (a), Wang and Gaetani (2008) (b), this study (c), and Wang and Gaetani (2008) (d).

Fig. 4S. D_{Mn}^{2+} values measured from magma-carbonate interaction experiments vs. those predicted by the models of Wang and Gaetani (2008) (a) and this study (b).

Fig. 5S. D_{Ni}^{2+} values measured from magma-carbonate interaction experiments vs. those predicted by the models of Snyder and Carmichael (1992) (a), Wang and Gaetani (2008) (b), and Pu et al. (2017) (c).

Fig. 6S. $K_{D(Fe-Mg)}$ values measured from magma-carbonate interaction experiments vs. those predicted by the models of Toplis (2005) (a), Putirka (2016) for ferric iron in the melt recalculated according to Kress and Carmichael (1991) (b), and Putirka (2016) for all iron in the melt treated as FeO_t (c).

Table 1. Experimental conditions and phase relations

Run (#)	Mg# melt	$CaCO_3$ (wt.%)	*t* (h)	T (°C)	P (MPa)	$\log(fO_2)$	Gl (wt.%)	Ol (wt.%)	Cpx (wt.%)	Ti-Mt (wt.%)
MM1-A	72	0	72	1250	0.1	-7.7	96.5	3.5	-	-
MM1-C	72	10	72	1250	0.1	-7.7	97.8	2.2	-	-
MM1-D	72	20	72	1250	0.1	-7.7	99.1	0.9	-	-
MM2-A	72	0	72	1200	0.1	-8.2	93.7	6.3	-	-
MM2-C	72	10	72	1200	0.1	-8.2	86.9	4.8	8.3	-
MM2-D	72	20	72	1200	0.1	-8.2	84.2	1.5	14.3	-
MM3-A	72	0	72	1150	0.1	-8.85	79.1	8.0	11.6	1.2
MM3-C	72	10	72	1150	0.1	-8.85	76.7	6.4	15.7	1.2
MM3-D	72	20	72	1150	0.1	-8.85	74.7	4.1	20.2	1.0
MM4-A	75	0	72	1250	0.1	-7.7	95.7	4.3	-	-
MM4-C	75	10	72	1250	0.1	-7.7	96.7	3.3	-	-
MM4-D	75	20	72	1250	0.1	-7.7	98.1	1.9	-	-
MM5-A	75	0	72	1200	0.1	-8.2	92.8	7.2	-	-
MM5-C	75	10	72	1200	0.1	-8.2	94.7	5.3	-	-
MM5-D	75	20	72	1200	0.1	-8.2	95.2	4.8	-	-
MM6-A	75	0	72	1150	0.1	-8.85	90.7	9.3	-	-
MM6-C	75	10	72	1150	0.1	-8.85	87.3	7.7	5.0	-
MM6-D	75	20	72	1150	0.1	-8.85	79.0	6.7	14.3	-
MM7-A	78	0	72	1250	0.1	-7.7	93.3	6.7	-	-
MM7-C	78	10	72	1250	0.1	-7.7	95.0	5.0	-	-
MM7-D	78	20	72	1250	0.1	-7.7	97.2	2.8	-	-
MM8-A	78	0	72	1200	0.1	-8.2	90.1	9.9	-	-
MM8-C	78	10	72	1200	0.1	-8.2	91.7	8.3	-	-
MM8-D	78	20	72	1200	0.1	-8.2	92.2	7.8	-	-
MM9-A	78	0	72	1150	0.1	-8.85	88.0	12.0	-	-
MM9-C	78	10	72	1150	0.1	-8.85	89.5	10.5	-	-
MM9-D	78	20	72	1150	0.1	-8.85	81.4	9.1	9.5	-

Research Highlights

Fo-CaO-rich, NiO-poor olivines crystallize from experimentally-derived melts assimilating up to 20 wt.% of carbonate. > The amount of Ca entering the crystal lattice is proportional to the Ca-O-Si bonds available in the melt structure. > D_{Ca}^{2+} and D_{Mg}^{2+} increase with increasing $CaCO_3$ assimilation, whereas D_{Fe}^{2+}, D_{Mn}^{2+}, and D_{Ni}^{2+} decrease. > The exchange partition coefficients between Fe^{2+}/Ca/Mn/Ni and Mg are primarily controlled by the melt structure. > The Fe^{2+}-Mg exchange invariably approaches to the equilibrium condition of 0.33±0.04.

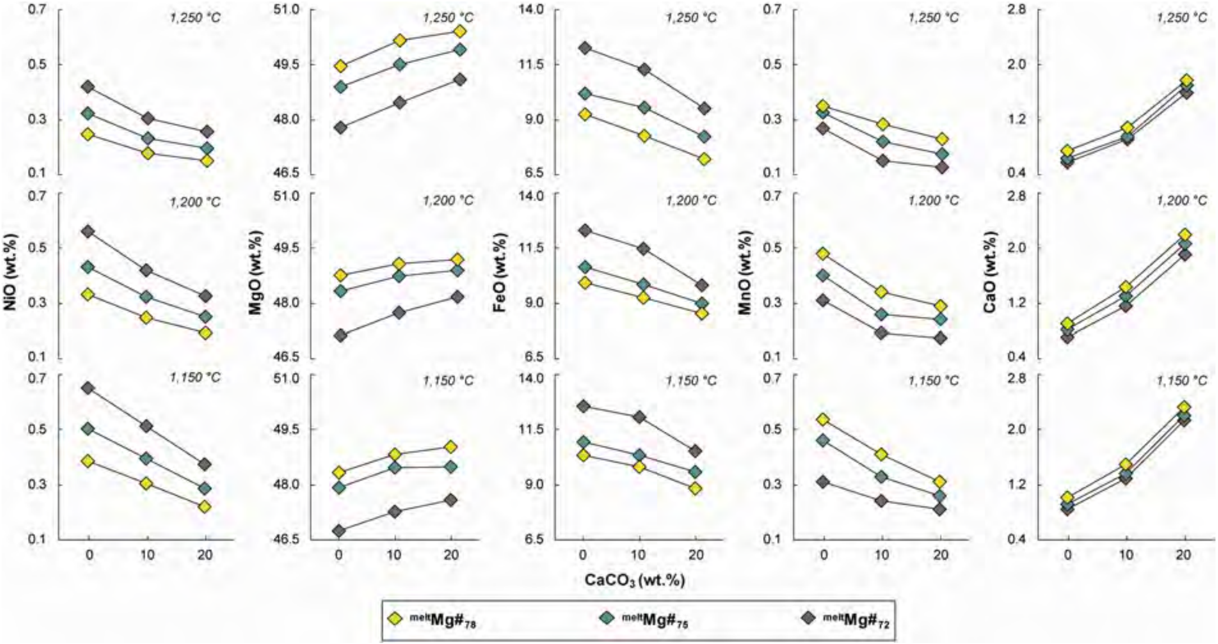
NiO (wt.%)
MgO (wt.%)
FeO (wt.%)
MnO (wt.%)
CaO (wt.%)
1,250 °C
1,200 °C
1,150 °C
0.7
0.5
0.3
0.1
51.0
49.5
48.0
46.5
14.0
11.5
9.0
6.5
2.8
2.0
1.2
0.4
0
10
20
$CaCO_3$ (wt.%)
$^{melt}Mg\#_{78}$
$^{melt}Mg\#_{75}$
$^{melt}Mg\#_{72}$

Figure 1

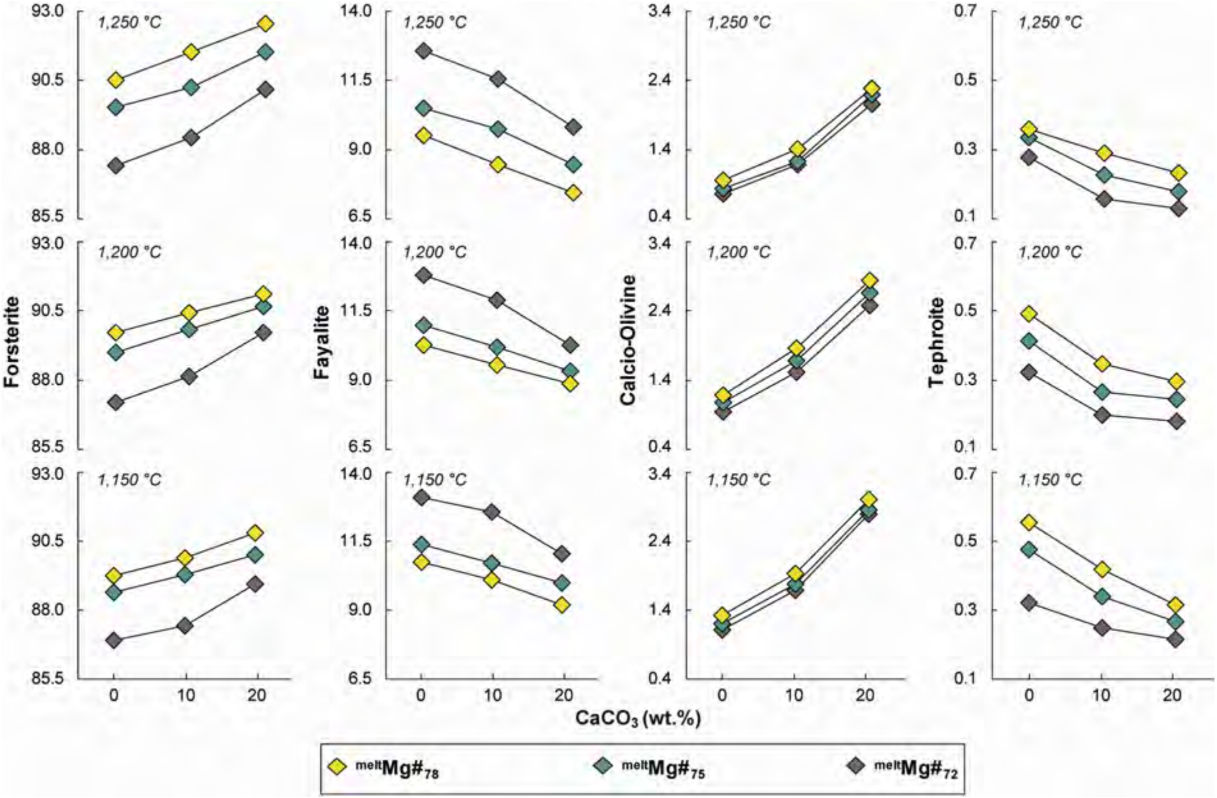

1,250 °C
1,200 °C
1,150 °C
Forsterite
Fayalite
Calcio-Olivine
Tephroite
93.0
90.5
88.0
85.5
14.0
11.5
9.0
6.5
3.4
2.4
1.4
0.4
0.7
0.5
0.3
0.1
0
10
20
CaCO₃ (wt.%)
meltMg#78
meltMg#75
meltMg#72

Figure 2

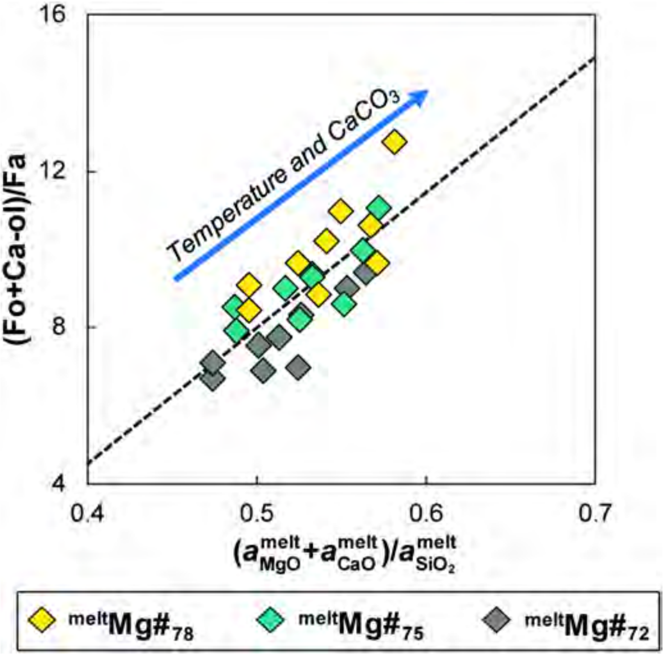
16
12
8
4
0.4
0.5
0.6
0.7
(Fo+Ca-ol)/Fa
$(a^{melt}_{MgO}+a^{melt}_{CaO})/a^{melt}_{SiO_2}$
Temperature and CaCO₃
◇ ${}^{melt}Mg\#_{78}$
◇ ${}^{melt}Mg\#_{75}$
◆ ${}^{melt}Mg\#_{72}$

Figure 3

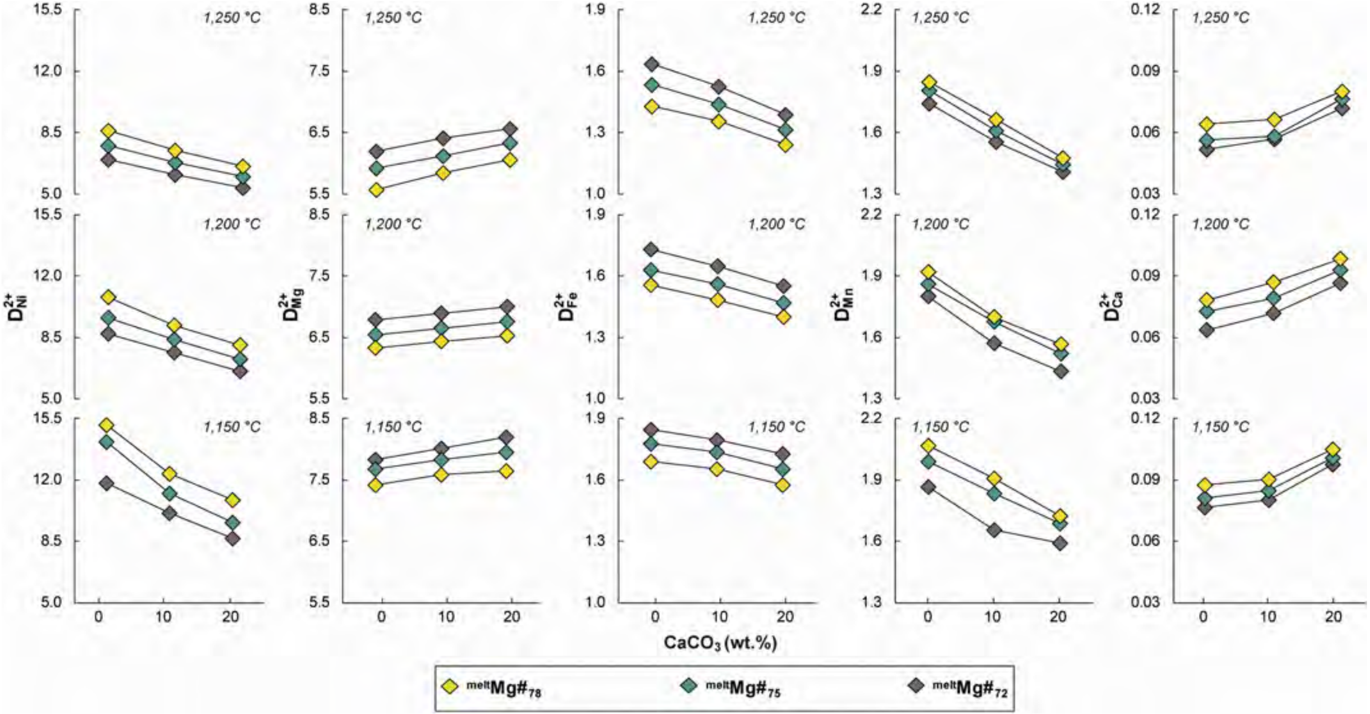
1,250 °C
1,200 °C
1,150 °C
D^{2+}_{Ni}
D^{2+}_{Mg}
D^{2+}_{Fe}
D^{2+}_{Mn}
D^{2+}_{Ca}
15.5
12.0
8.5
5.0
8.5
7.5
6.5
5.5
1.9
1.6
1.3
1.0
2.2
1.9
1.6
1.3
0.12
0.09
0.06
0.03
0
10
20
$CaCO_3$ (wt.%)
$^{melt}Mg\#_{78}$
$^{melt}Mg\#_{75}$
$^{melt}Mg\#_{72}$

Figure 4

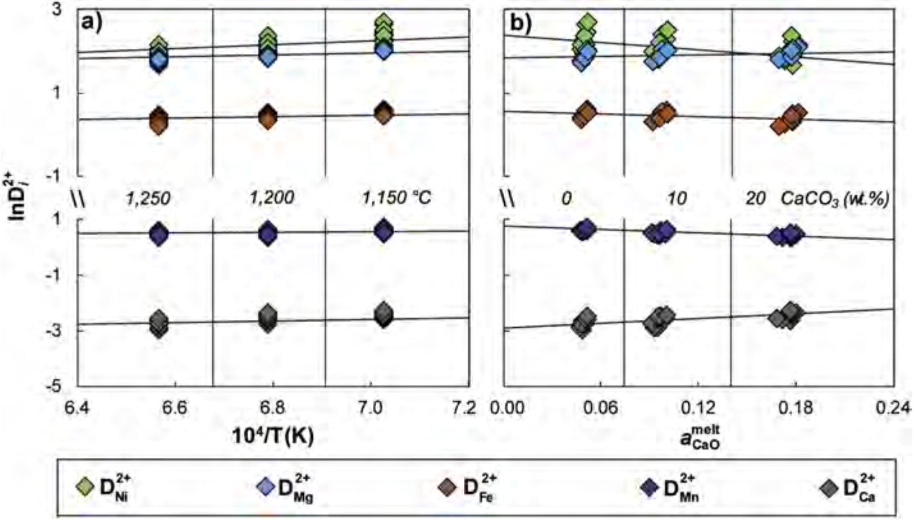a)
b)
$\ln D_i^{2+}$
3
1
-1
1
-1
-3
-5
1,250
1,200
1,150 °C
0
10
20
CaCO$_3$ (wt.%)
6.4
6.6
6.8
7.0
7.2
0.00
0.06
0.12
0.18
0.24
10^4/T(K)
a_{CaO}^{melt}
D_{Ni}^{2+}
D_{Mg}^{2+}
D_{Fe}^{2+}
D_{Mn}^{2+}
D_{Ca}^{2+}

Figure 5

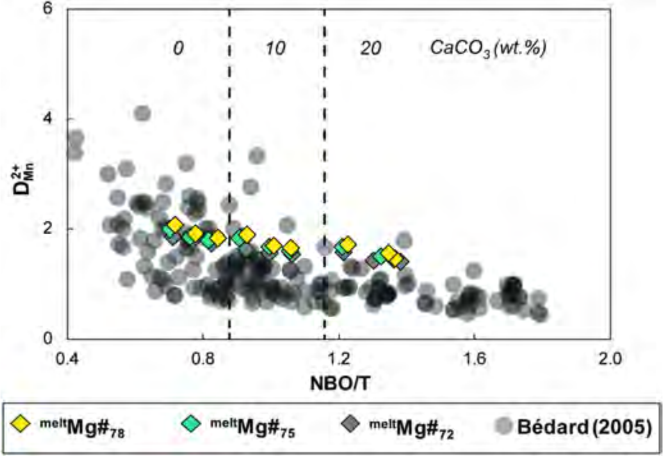
6
4
2
0
D^{2+}_{Mn}
0
10
20
$CaCO_3$ (wt.%)
0.4
0.8
1.2
1.6
2.0
NBO/T
$^{melt}Mg\#_{78}$
$^{melt}Mg\#_{75}$
$^{melt}Mg\#_{72}$
Bédard (2005)

Figure 6

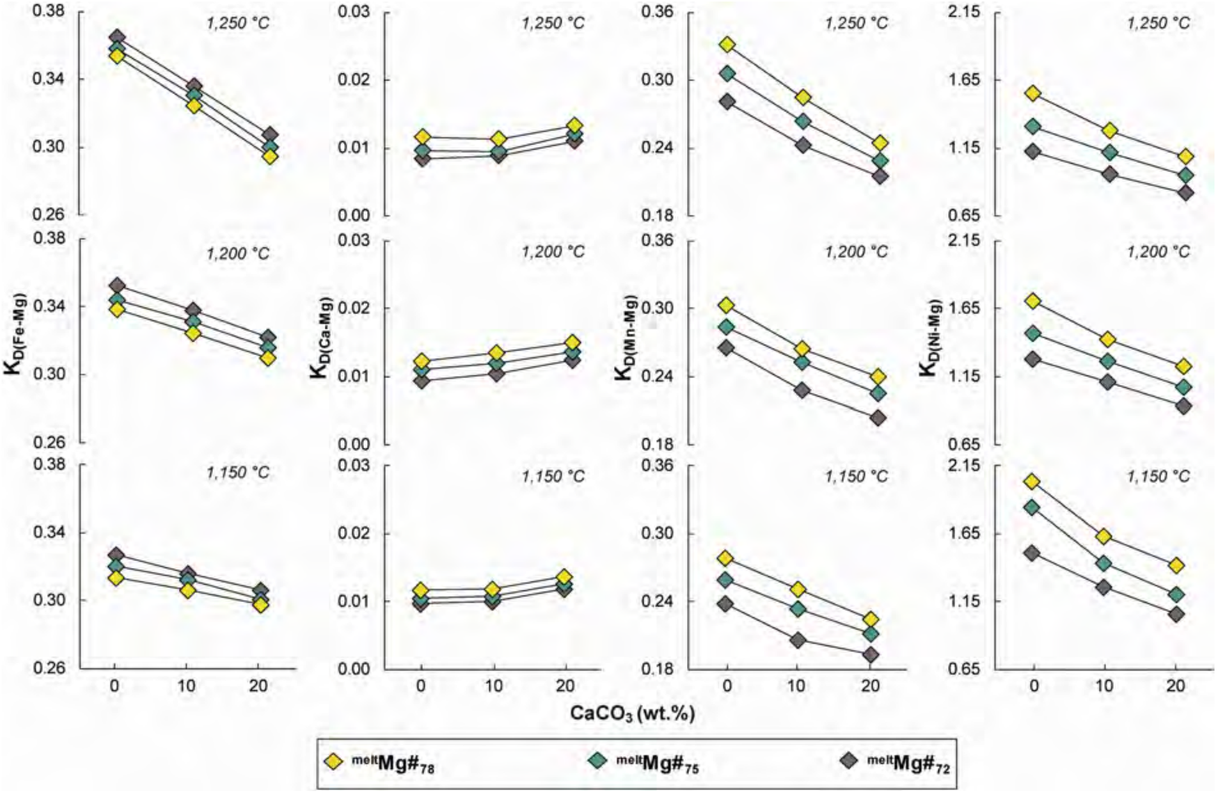

1,250 °C
1,200 °C
1,150 °C
$K_{D(Fe\text{-}Mg)}$
$K_{D(Ca\text{-}Mg)}$
$K_{D(Mn\text{-}Mg)}$
$K_{D(Ni\text{-}Mg)}$
0.38
0.34
0.30
0.26
0.03
0.02
0.01
0.00
0.36
0.30
0.24
0.18
2.15
1.65
1.15
0.65
0
10
20
$CaCO_3$ (wt.%)
$^{melt}Mg\#_{78}$
$^{melt}Mg\#_{75}$
$^{melt}Mg\#_{72}$

Figure 7

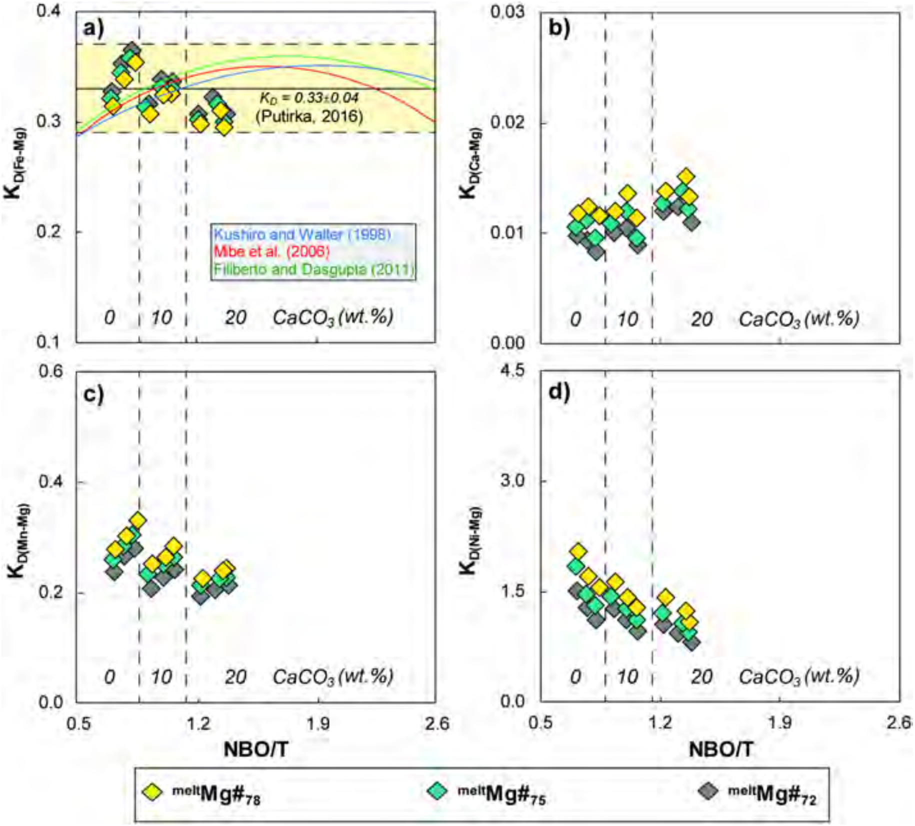
a)
b)
c)
d)
$K_{D(Fe\text{-}Mg)}$
$K_{D(Ca\text{-}Mg)}$
$K_{D(Mn\text{-}Mg)}$
$K_{D(Ni\text{-}Mg)}$
0.4
0.3
0.2
0.1
0.03
0.02
0.01
0.00
0.6
0.4
0.2
0.0
4.5
3.0
1.5
0.0
$K_D = 0.33 \pm 0.04$
(Putirka, 2016)
Kushiro and Walter (1998)
Mbe et al. (2006)
Filiberto and Dasgupta (2011)
0
10
20
$CaCO_3$ (wt.%)
0.5
1.2
1.9
2.6
NBO/T
$^{melt}Mg\#_{78}$
$^{melt}Mg\#_{75}$
$^{melt}Mg\#_{72}$

Figure 8

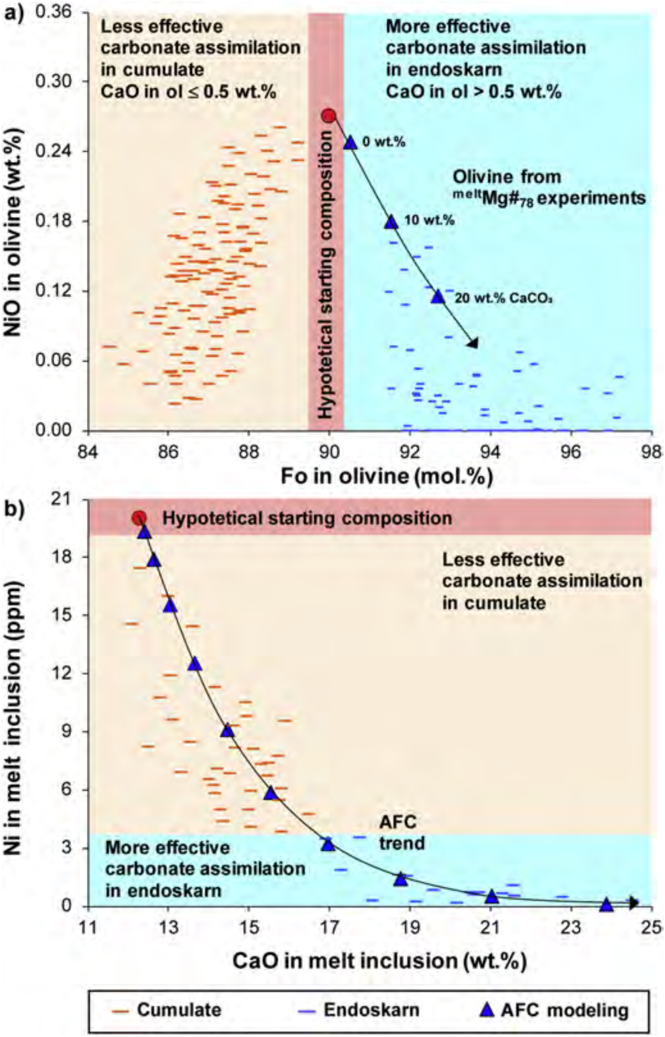
a)
0.36
0.30
0.24
0.18
0.12
0.06
0.00
NiO in olivine (wt.%)
84
86
88
90
92
94
96
98
Fo in olivine (mol.%)
Less effective carbonate assimilation in cumulate CaO in ol ≤ 0.5 wt.%
More effective carbonate assimilation in endoskarn CaO in ol > 0.5 wt.%
Hypotetical starting composition
0 wt.%
10 wt.%
20 wt.% CaCO₃
Olivine from meltMg#78 experiments
b)
21
18
15
12
9
6
3
0
Ni in melt inclusion (ppm)
11
13
15
17
19
21
23
25
CaO in melt inclusion (wt.%)
Hypotetical starting composition
Less effective carbonate assimilation in cumulate
More effective carbonate assimilation in endoskarn
AFC trend
Cumulate
Endoskarn
AFC modeling

Figure 9

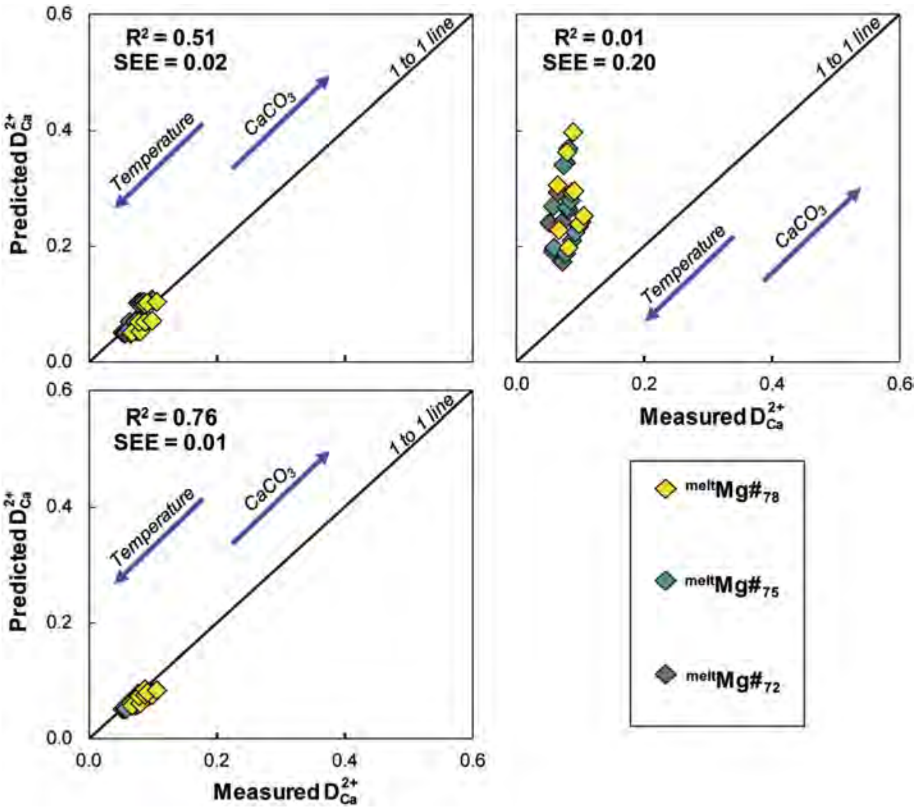

$R^2 = 0.51$
SEE = 0.02
$R^2 = 0.01$
SEE = 0.20
$R^2 = 0.76$
SEE = 0.01
1 to 1 line
Temperature
$CaCO_3$
Predicted D_{Ca}^{2+}
Measured D_{Ca}^{2+}
0.0
0.2
0.4
0.6
$^{melt}Mg\#_{78}$
$^{melt}Mg\#_{75}$
$^{melt}Mg\#_{72}$

Figure 10

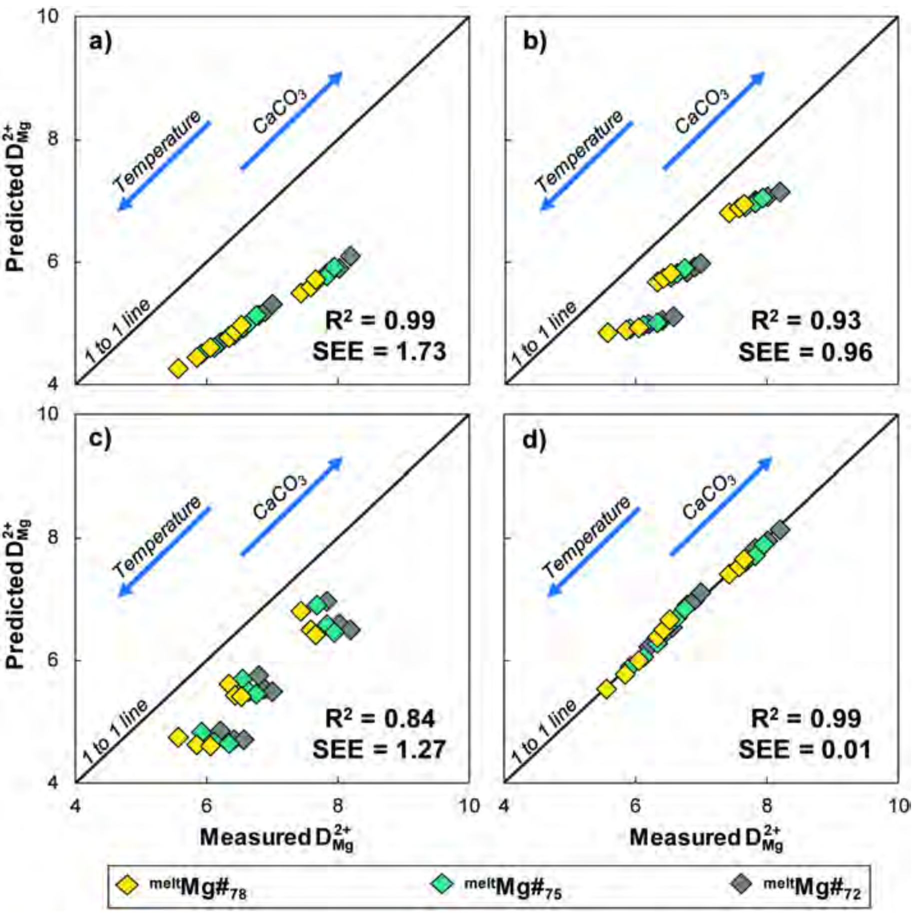
a)
b)
c)
d)
Predicted D^{2+}_{Mg}
Measured D^{2+}_{Mg}
Temperature
$CaCO_3$
1 to 1 line
$R^2 = 0.99$
SEE = 1.73
$R^2 = 0.93$
SEE = 0.96
$R^2 = 0.84$
SEE = 1.27
$R^2 = 0.99$
SEE = 0.01
4
6
8
10
${}^{melt}Mg\#_{78}$
${}^{melt}Mg\#_{75}$
${}^{melt}Mg\#_{72}$

Figure 11

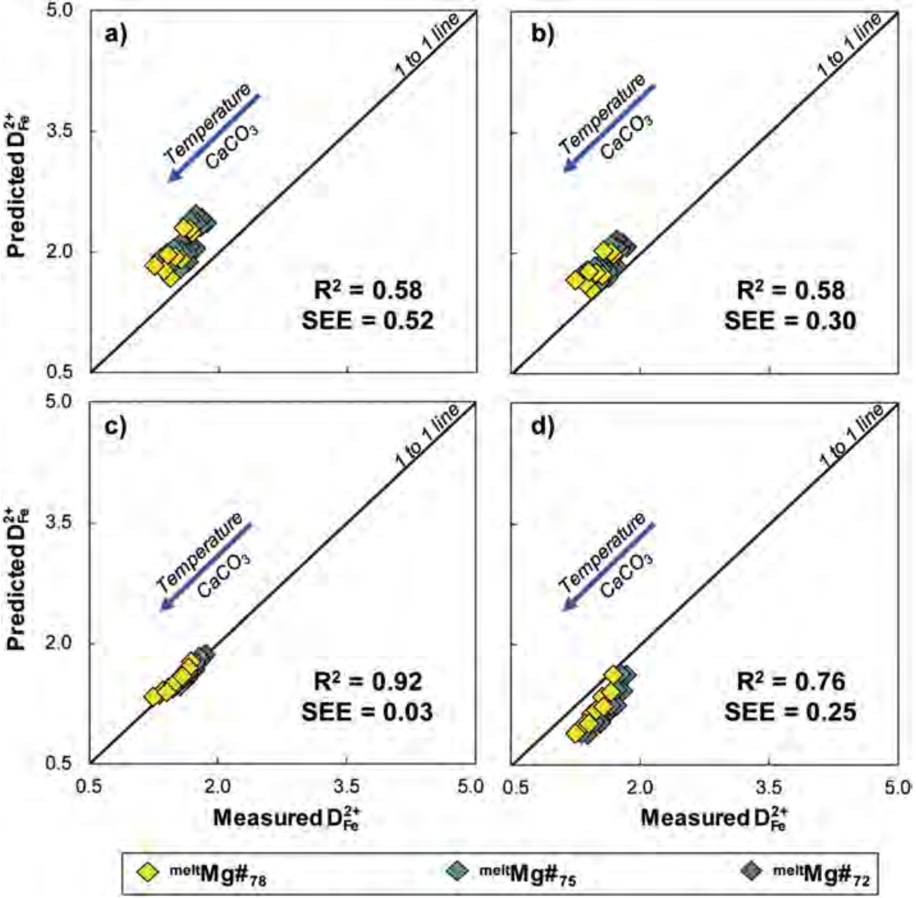
a)
b)
c)
d)
1 to 1 line
Temperature
$CaCO_3$
$R^2 = 0.58$
SEE = 0.52
$R^2 = 0.58$
SEE = 0.30
$R^2 = 0.92$
SEE = 0.03
$R^2 = 0.76$
SEE = 0.25
Predicted D_{Fe}^{2+}
Measured D_{Fe}^{2+}
0.5
2.0
3.5
5.0
$^{melt}Mg\#_{78}$
$^{melt}Mg\#_{75}$
$^{melt}Mg\#_{72}$

Figure 12

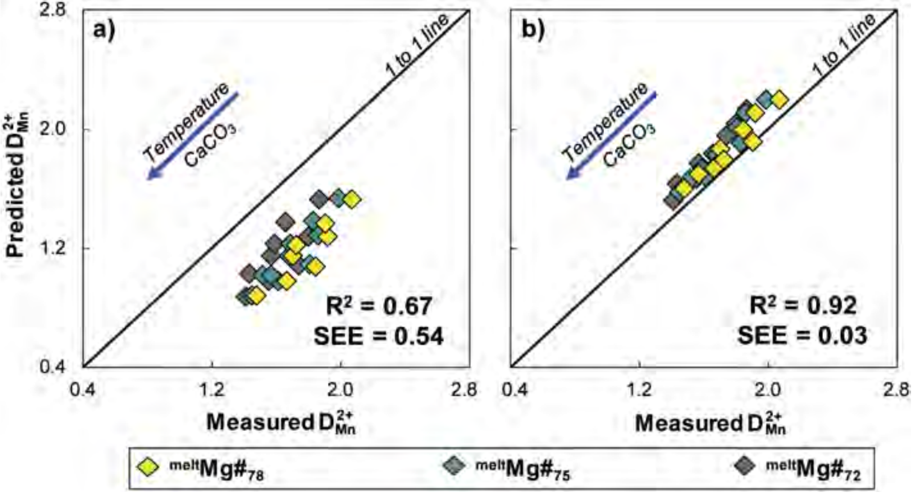
a)
b)
1 to 1 line
1 to 1 line
Temperature
CaCO$_3$
Temperature
CaCO$_3$
R^2 = 0.67
SEE = 0.54
R^2 = 0.92
SEE = 0.03
Predicted D^{2+}_{Mn}
Measured D^{2+}_{Mn}
Measured D^{2+}_{Mn}
0.4
1.2
2.0
2.8
0.4
1.2
2.0
2.8
0.4
1.2
2.0
2.8
^{melt}Mg#$_{78}$
^{melt}Mg#$_{75}$
^{melt}Mg#$_{72}$

Figure 13

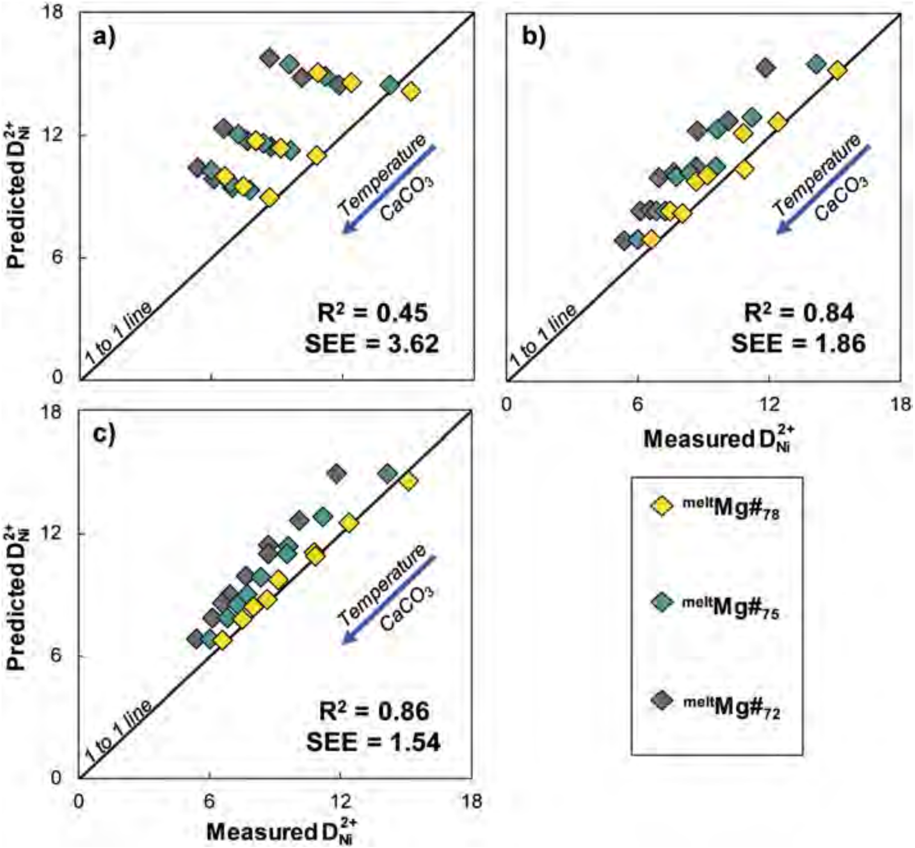
a)
b)
c)
Predicted D_{Ni}^{2+}
Measured D_{Ni}^{2+}
0
6
12
18
1 to 1 line
Temperature
$CaCO_3$
$R^2 = 0.45$
SEE = 3.62
$R^2 = 0.84$
SEE = 1.86
$R^2 = 0.86$
SEE = 1.54
$^{melt}Mg\#_{78}$
$^{melt}Mg\#_{75}$
$^{melt}Mg\#_{72}$

Figure 14

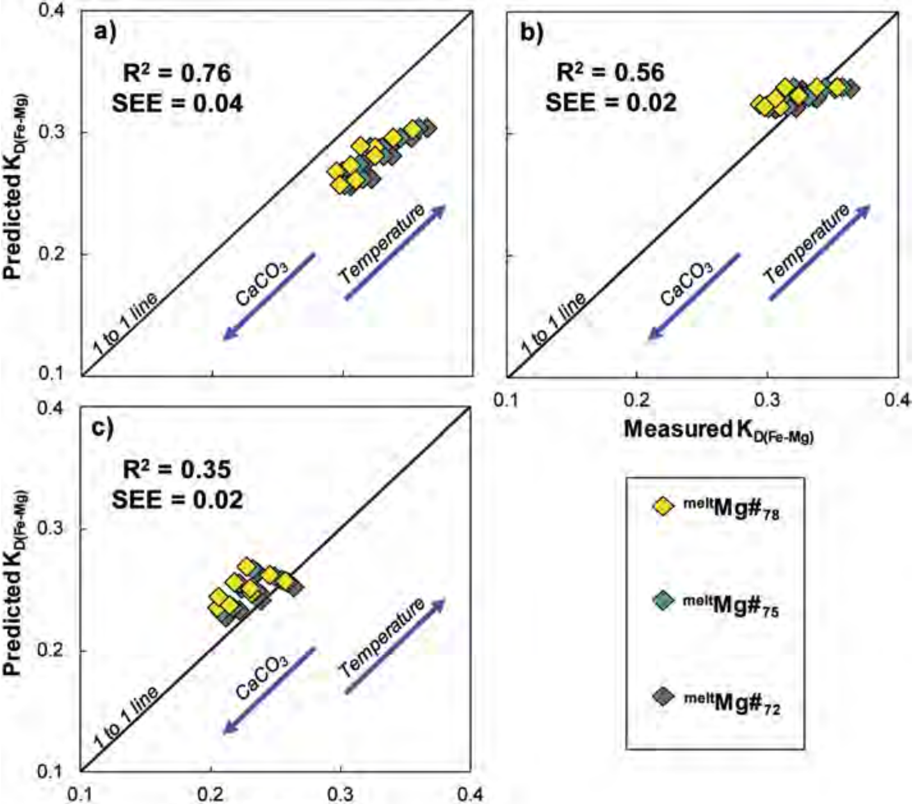
a)
R² = 0.76
SEE = 0.04
b)
R² = 0.56
SEE = 0.02
c)
R² = 0.35
SEE = 0.02
1 to 1 line
CaCO3
Temperature
Predicted K D(Fe-Mg)
Measured K D(Fe-Mg)
0.1
0.2
0.3
0.4
meltMg#78
meltMg#75
meltMg#72

Figure 15